JP0050833

A GLOBAL MHD MODEL OF THE JOVIAN MAGNETOSPHERE

September 2000

Takahiro MIYOSHI and Kanya KUSANO*

A Global MHD Model of the Jovian Magnetosphere

Takahiro MIYOSHI and Kanya KUSANO*

Department of Fusion Plasma Research
Naka Fusion Research Establishment
Japan Atomic Energy Research Institute
Naka-machi, Naka-gun, Ibaraki-ken

A new global model of the Jovian magnetosphere is proposed by using the magnetohydrodynamic (MHD) simulation, in which the interaction between a rapidly rotating magnetosphere and the external plasma flow is investigated. In this study, the steady solar wind with/without the interplanetary magnetic filed (IMF) is applied on the inflow boundary. The results clearly indicate that the global structure of the magnetic field lines of force is largely affected by the rotation of Jupiter as well as by the solar wind. It is also found that magnetic reconnection at the tail region generates the plasma outflow and greatly modifies the corotational structure of the plasmas in the magnetosphere. Especially when the relatively high speed solar wind or the solar wind with the northward IMF collides on the magnetosphere, strong magnetic reconnection at the tail induces the tail-dusk flow, which is against the corotation. On the other hand, the evident tail dusk flow does not appear in the case of the low speed solar wind or the case with the southward IMF. Thus, the internal structure of the rotating magnetosphere will be altered even qualitatively in response to the solar wind parameters.

* Hiroshima University

木星磁気圏の大域的MHDモデル

日本原子力研究所那珂研究所炉心プラズマ研究部

三好 隆博・草野 完也*

(2000 年 7 月 3 日 受理)

　　本論文では、高速回転する磁気圏と高速プラズマ流との非線形相互作用に関する磁気流体力学 (MHD) シミュレーションに基づき、新たな大域的木星磁気圏モデルを提案する。特に本研究では、高速プラズマ流の流入境界条件として、惑星間空間磁場 (IMF) を含有する、または含有しない定常太陽風を仮定する。シミュレーション結果より、木星磁気圏の大域的磁力線構造は、太陽風と同時に、木星自身の高速自転に大きな影響を受けていることがはっきりと示される。また、磁気圏尾部における磁気再結合が、磁気圏内のプラズマ対流構造に大きな影響を与えていることが明らかにされる。これらの構造は、太陽風動圧の強度や IMF の極性など太陽風パラメータの僅かな変化に応答し、定性的にも変化することが指摘される。

那珂研究所：〒 311-0193 茨城県那珂郡那珂町向山 801-1

*広島大学

Contents

目　　次

1. Introduction

Flybys of previous five spacecraft before the arrival of the Galileo orbiter spacecraft have enlightened abundant distinctive features of the Jovian magnetosphere despite momentary observations along the specified trajectories. The in-situ observations of the magnetic field indicated that the Jovian magnetosphere is divided into three portions, such as the inner magnetosphere with the dipole-dominant magnetic field, the middle magnetosphere with the current disc-induced azimuthal magnetic field, and the outer magnetosphere with the southward magnetic field [1]. Also, it was detected at the middle magnetosphere that denser and cooler plasmas are confined in a thin disc-like region which corresponds to the current disc [2]. Furthermore, multiple time crossing signals for the bow shock and the magnetopause were measured at the various radii, which imply the sponginess of the day side Jovian magnetosphere [3,4]. It was also reported that the Ulysses outbound flyby, in which the trajectory traversed the dusk meridian with the southerly inclination of the middle latitude unlike other spacecraft [5], may pass the cusp of the Jovian magnetosphere [6]. In addition to these fruits, the Galileo orbiter could present more detail information within a wide area during a long time interval, such as long periodic modulations of the Jovian magnetosphere in several days [7,8]. Besides, the outflow bursts, which are thought as the different events from the magnetospheric wind via Voyager observations [9], was newly observed at the premidnight-predawn region [10].

It was theoretically insisted that the magnetospheric rotation has the significant corotation lag, which is caused not only by the Pedersen conductivity of the ionosphere but also by the outward plasma transport [11]. Here, the outward transport itself is considered to be stimulated by the interchange instability (e.g., [12], and references therein). Indeed, an expected lag was detected by in-situ observations in the inner and the middle Jovian magnetosphere [2,13]. On the other hand, in an early picture of the global Jovian magnetosphere, *Brice and Ioannidis* [14] argued on the global plasma convection dominated by the corotation with Jupiter rather than the solar wind-driven convection in contrast with the Earth's magnetosphere. Subsequently, several improved models were proposed, in those the plasma outflow from the inner magnetosphere as well as the corotation was taken into account (e.g., [15]). Their idea was such that the magnetospheric wind is produced beyond a critical radius R_A, where the kinetic energy of the corotation exceeds the magnetic energy; i.e., the corotational speed is match for the local Alfvén speed V_A there. Though the existence of the outflow was suggested at the postmidnight region beyond about $100R_J$, it was found that the plasmas almost corotate at the prenoon region by the Voyager observations [9]. Therefore, *Vasyliunas* [16] proposed the model such that the outflow may occur via magnetic reconnection in the tail region while the plasmas are accelerated to the corotational sense at the day side magnetosphere. *Cheng and Krimigis* [17] also constructed a conceptual model of a global flow pattern based on the Voyager observations. *Cowley et al.* [18] presented a model based on the Ulysses observations, in which several previous models, such as the Hill's model [11] at the inner magnetosphere, and the Vasyliunas' model [16] at the tail region, are included. Quite recently, first global magnetohydrodynamic (MHD) simulations of the Jovian magnetosphere were independently performed by *Miyoshi and Kusano* [19] and *Ogino et al.* [20]. In both models, the plasma disc-like structure, and the plasma convection including the flow induced by tail reconnection were realized in a similar manner.

In this paper, to investigate the global structure of the Jovian magnetosphere, detail analyses of the nonlinear interaction between a rapidly rotating magnetosphere and the external plasma flow will be presented in a scope of the MHD description. The simulations are carried out for several cases, those have different parameters for solar wind; dynamic pressure and orientation of the interplanetary magnetic field (IMF). Finally, a global Jovian magnetospheric MHD model, especially for a middle to an outer region, will be proposed. In the following section, the present simulation model is explained. The simulation results are analyzed in detail for typical cases,

in section 3. Three dimensional global picture of the Jovian magnetosphere will be presented, in section 4. Finally, some important results in this paper are summarized in section 5.

2. Simulation Model

In the magnetospheric simulations, the MHD equations are widely used in order to describe macroscopic picture as inferred from the Earth's global MHD simulations (e.g., [21], and references therein). Also in our model, we adopt the MHD equations as the basic equations since an MHD model seems to be suitable for constructing the global model of the Jovian magnetosphere as the first approximation. Some difficulty for the global magnetospheric MHD simulation, however, arises from the fact that an intrinsic potential field of a planet $\mathbf{B}_p$ rapidly decreases as a function of the distance from the planet in several orders of magnitude. On the other hand, the fluctuating components from the potential field may have almost same order of the magnitude in the whole magnetosphere. Therefore, we numerically solve the following equations, in those the contributions of the potential field are excluded from the state vector $\mathbf{U} = (\rho, \rho\mathbf{V}, \mathbf{B}, \varepsilon)^T$ of the standard MHD equations [22,23]:

$$\frac{\partial \tilde{\mathbf{U}}}{\partial t} + (\nabla \cdot \tilde{\mathbf{F}})^T = 0, \tag{1}$$

where

$$\tilde{\mathbf{U}} = \begin{pmatrix} \rho \\ \rho\mathbf{V} \\ \tilde{\mathbf{B}} \\ \tilde{\varepsilon} \end{pmatrix}, \tag{1a}$$

$$\tilde{\mathbf{F}} = \begin{pmatrix} \rho\mathbf{V} \\ \rho\mathbf{V}\mathbf{V} + (P + \frac{B^2}{2\mu_0} - \frac{B_p^2}{2\mu_0})\mathbf{I} - (\frac{\mathbf{B}\mathbf{B}}{\mu_0} - \frac{\mathbf{B}_p\mathbf{B}_p}{\mu_0}) \\ \mathbf{V}\mathbf{B} - \mathbf{B}\mathbf{V} \\ (\tilde{\varepsilon} + \frac{\tilde{B}^2}{2\mu_0} + P)\mathbf{V} - \frac{\tilde{\mathbf{B}}(\tilde{\mathbf{B}}\cdot\mathbf{V})}{\mu_0} + \frac{(\tilde{\mathbf{B}}\cdot\mathbf{B}_p)\mathbf{V}}{\mu_0} - \frac{\mathbf{B}_p(\tilde{\mathbf{B}}\cdot\mathbf{V})}{\mu_0} \end{pmatrix}^T, \tag{1b}$$

and $\tilde{\mathbf{B}} = \mathbf{B} - \mathbf{B}_p$, $\tilde{\varepsilon} = \varepsilon - \mathbf{B}_p \cdot \tilde{\mathbf{B}}/\mu_0 - B_p^2/2\mu_0$. In the above equations, ρ, $\mathbf{V}$, $\mathbf{B}$, ε, P, $\mathbf{I}$, μ_0, and γ denote the plasma density, the bulk velocity, the magnetic field, the total energy density, the plasma pressure, the unit matrix, the permeability, and the adiabatic constant, respectively. The dissipative effects relating to the viscous, the resistive and the heat conductive terms are not explicitly included, because our primary objective is the qualitative construction of the global Jovian magnetospheric model rather than the quantitative analysis for the dependence of the dissipative coefficients. The relation between the pressure and the fluctuating components is given by

$$P = (\gamma - 1)\left(\tilde{\varepsilon} - \frac{\rho V^2}{2} - \frac{\tilde{B}^2}{2\mu_0}\right). \tag{1c}$$

It is obvious that the modified form of the MHD equations (1) has the same form as the standard equations if $\mathbf{B}_p = 0$.

In order to capture discontinuities appearing in the magnetospheric system sharply, we apply the total variation diminishing (TVD) scheme to the above MHD equations. The TVD scheme of multidimensional MHD equations, however, cannot be constructed straightforwardly because the upwind-weighted finite difference (volume) scheme based on the one dimensional MHD Riemann problem, i.e., seven-waves characteristic equations [24], breaks the divergence free condition of the magnetic field in multidimensions. In order to overcome this shortage, the projection scheme has been used in the typical previous simulations, where an additional Poisson equation must be solved (e.g., [22,23,25]). As another manner, *Powell* [26] and *Gombosi*

et al. [27,28] recently developed a new straightforward approach based on the eight-waves characteristic form of the MHD equations. In this approach, the magnetic field normal to a surface of the control volume can be evolved with time. Here, according to *Powell* [26], *Gombosi et al.* [27,28], the present form of the equations (1) is modified to the following form:

$$\frac{\partial \tilde{U}}{\partial t} + (\nabla \cdot \tilde{F})^T = \tilde{S}, \tag{2}$$

where

$$\tilde{S} = - \begin{pmatrix} 0 \\ \frac{1}{\mu_0}B \\ V \\ \frac{1}{\mu_0}V \cdot \tilde{B} \end{pmatrix} \nabla \cdot \tilde{B}. \tag{2a}$$

The eigenvalues and eigenvectors of this form coincide not only with those obtained by *Powell* [1994] when $B_p = 0$ but also with those derived by *Tanaka* [1994] when the normal component of the magnetic field is constant. This set of equations is numerically solved by applying the second-order finite volume TVD scheme, where the second-order accuracy is realized by the variable extrapolation with minmod limiter [29].

Since we focus on the global structure in the middle and the outer portion of the Jovian magnetosphere, the simulation domain is given by a large rectangular box, $(-350R_J, -250R_J, 0) \leq (x,y,z) \leq (150R_J, 250R_J, 250R_J)$, in which the inner half sphere of the radius $r_0 = 30R_J$ is clipped off. Here we use the solar-magnetospheric coordinate, where the x, y and z point to the sun, the dusk and the north, respectively. The grid structure adopted here is shown in Figure 1, where the radial grid size varies about from $0.6R_J$ to $33.6R_J$ with the distance from the origin in order to describe a fine structure appearing near the inner boundary.

Our simulation model consists of four types of the boundary condition as follows: The mirror boundary condition is adopted at the equatorial plane. The boundary condition on the top, the side and the tail boundaries are given by the free boundary condition where the radial derivative of all physical quantities is fixed to zero. The inflow parameters at the front boundary are shown in Table 1 for each simulation run, in all cases the steady supersonic/super-Alfvénic inflow being applied. As discussed in the previous paper [19], we treat the inner boundary at r_0 simply as a plasma bath since it is expected that, in the middle and the outer portion of the Jovian magnetosphere, the mass transport is mainly governed by a large scale MHD convection rather than small scale instabilities at the Io torus. Indeed, it has been suggested that the time scale of the plasma transport from the Io torus by the interchange instability is an order of days to months [30,31]. Thus, in the current model, the inner boundary condition of the density and the pressure is switched depending on the sign of the radial component of the velocity V_r, such that $\rho = n_0 m_i$, $P = P_0$ for $V_r > 0$, and $\partial \rho/\partial r = 0$, $\partial P/\partial r = 0$ for $V_r \leq 0$, where m_i is the mass of proton, $n_0 = 0.1/\mathrm{cm}^3$ and $P_0 = 1.1 \times 10^{-12}\mathrm{erg/cm}^3 (\approx 2P_{SW})$, respectively. These parameters n_0 and P_0 are chosen from in-situ measurements at the middle portion of the Jovian magnetosphere [32]. The velocity parallel to the magnetic field, $V_{\parallel} = V \cdot B/B$, at the inner boundary is determined such as to satisfy the relation $\partial(r^2\rho V_{\parallel})/\partial r = 0$. The velocity perpendicular to the magnetic field, $V_\perp = V - V_{\parallel}B/B$, is determined by $V_\perp = E \times B/B^2$, where $E = -(\Omega_0 \times r_0) \times B$. The angular velocity Ω_0 at r_0 is set to a half of the Jovian angular velocity, $\Omega_J = (2\pi/10.0)e_z /\mathrm{h}$, based on the observation in the inner to the middle Jovian magnetosphere [2,13]. The lag from the rigid corotation with Jupiter was basically explained by *Hill*'s model [11].

The intrinsic potential field of Jupiter is represented by the dipole field, $B_p = B_J R_J^3 \{3(e_z \cdot e_r)e_r - e_z\}/r^3$, where B_J is the intensity of the magnetic field at the equatorial surface of Jupiter $(4.7 \times 10^{-4}\mathrm{T})$. The initial configuration of the magnetic field is constructed by the superposition of two dipole fields those are located at the origin and the mirror symmetric position for the front

of the simulation domain, i.e., $(x, y, z) = (300R_J, 0, 0)$, such that the perpendicular component is vanished on the day side boundary [33]. The potential flow tangent to a sphere of the radius $r_1 = 50R_J$, which is almost the distance of the magnetopause for the case without the rotation, is initially imposed in order to achieve the quasi-steady state quickly. The rotational flow is also superposed, where the angular velocity Ω is assumed to decrease smoothly from the rigid rotation: $\Omega = \{1 - \tanh[(r - r_1)/\Delta]\}\Omega_0/2$ where $\Delta = 5R_J$. The density and the pressure are initially given as $\rho = m_i n_0$ and $P = P_0$ in the whole domain, respectively.

3. Simulation Results

In each run, the quasi-steady states are achieved in $t \approx 70h$ when the inner sphere has rotated about three and a half times and the solar wind has traveled more than $1000R_J$. By observing those quasi-steady states, we investigate the global structure of the rotating magnetosphere and the dependence on the solar wind parameters. First of all, the fundamental structure of the rotating magnetosphere interacting with the plasma flow is presented, especially in the cases without the IMF, in detail. Subsequently, the interaction to the solar wind with the northward/southward IMF will be investigated.

3.1. Cases Without IMF

Figure 2 displays the global structure of the magnetic field lines of force in the case L, that structure is largely affected by the rotation as well as by the solar wind. Here the green lines are the magnetic field lines of force traced from the inner sphere and the yellow lines are detached from the inner sphere. Also, the purple line at the equatorial plane indicates the magnetic neutral line. It is found at once that the magnetic field lines of force rooted to the high latitudinal inner sphere are helically twisted due to the planetary rotation. On the other hand, the low latitudinal magnetic field lines of force seem to be closed in the day side portion of the magnetosphere like the Earth's magnetosphere. Besides, the solar wind compresses the magnetosphere and forms the shape of the magnetotail. Therefore, the structure of the cusp, which is a boundary region between the closed and the open magnetic field lines of force, is generated. Here the open lines reach the tail boundary while the closed lines pass through the equatorial plane. Also, the existence of the isolated lines (yellow) at the tail region implies that magnetic reconnection takes place. The global structure of the magnetic field lines of force also for the case H is basically similar to that for the case L.

Also, Figure 3 shows the global convection pattern and the density distribution in the equatorial plane for the case L. Here, redder regions indicate the higher density regions while bluer regions are lower. The purple line also indicates the magnetic neutral line as in Figure 2. We find at once that the solar wind is stagnant and the density rises up at the front of the magnetosphere. It is also found that plasmas in the middle magnetosphere almost corotate around Jupiter, where the highest density region is constructed as a crescent at the dawn side of the sphere. On the other hand, the outward flows, which must be induced by magnetic reconnection as mentioned above, appear in the distant magnetotail.

3.1.1. High Latitudinal Structure

One of the prominent features in the present simulation is the spiral structure of the open magnetic field lines of force at the high latitudinal region as seen in Figure 2. *Dessler and Juday* [34] first considered that a coupling of the solar wind with the rotating planet may cause the helical configuration in the magnetotail. Then, *Isbell et al.* [35] proposed that the twisting angle might be determined by the relation between the rotational speed $r_T\Omega_0$ and the speed of

the solar wind in the upwind of the bow shock V_{SW}, where r_T is the radius of the magnetotail.

In our simulation, the helical magnetic field lines of force traced from the same latitude θ seem to form a flux surface shown in Figure 4. Particularly, the magnetic field line of force traced from the pole ($\theta = 90°$) may correspond to the magnetic axis of the flux surfaces, as illustrated in Figure 5a. Therefore, as a measure of the helical twist, we define the average pitch angle α of the magnetic field on the flux surface, as follows:

$$\alpha(\overline{r_T}, z_T) = \cos^{-1}\overline{\left(\frac{\mathbf{B}(0,\phi_T,z_T) \cdot \mathbf{B}(r_T,\phi_T,z_T)}{B(0,\phi_T,z_T)B(r_T,\phi_T,z_T)}\right)}, \tag{3}$$

where the flux surface is projected to a cylinder whose axis corresponds to a line rooted to the pole, as illustrated in Figure 5b. Here, r_T, ϕ_T, and z_T are the radius of the high latitudinal magnetotail from the magnetic axis, the left-handed azimuthal (longitudinal) coordinate, and the distance along the magnetic axis, respectively, in a cylindrical approximation of Figure 5b. In the definition (3), the bar denotes the average over an angle of ϕ_T on the intersection of the flux surface on the plane perpendicular to the magnetic axis. Thus, not only $\overline{r_T}$ (hereafter we replace $\overline{r_T}$ with r_T) but also α is regarded as a function of θ, which is the latitude on the root of the line. In the following analyses, we investigate only the distant magnetotail farther than $x = -100R_J$ since the cylindrical approximation is inadequate near the pole due to the bending effect of the magnetic field lines of force. Thus, we select the origin of the cylinder at $O_T = (-100R_J, y_{\mathrm{axis}}R_J, z_{\mathrm{axis}}R_J)$ for both cases H and L.

Figures 6a and 6b show the dependence of α on z_T for several flux surfaces specified by some latitudes in the cases H and L, respectively. In the case L, the pitch angle specified by θ is hardly varied far beyond the magnetotail of $-100R_J$. On the other hand, α in the case H gradually increases and reaches to the same level of the case L at the deeply distant magnetotail around $z_T \gtrsim 150R_J$ ($x \lesssim -250R_J$), except on the low latitudinal flux surface ($\theta = 65°$) which may be affected by some process on the magnetosheath. Thus, it is thought that, at the distant magnetotail, the twisting angle may not depend on the solar wind speed.

In order to verify above statement, in Figure 7, $\tan\alpha$, which indicates the ratio of B_{ϕ_T} to B_{z_T}, is plotted as a function of the radius r_T for the case L around the point $(-250R_J, -30R_J, 110R_J)$ marked by a circle in Figure 4. The ratio of the rotational speed to the solar wind speed, $r_T\Omega_0/V_{SW}$, as well as the ratio to the local Alfvén speed, $r_T\Omega_0/V_A$, are also plotted by the dotted and chain-dotted lines, respectively. The result clearly indicates that $\tan\alpha$ well agrees with $r_T\Omega_0/V_A$ rather than the prediction by *Isbell et al.* [35], $r_T\Omega_0/V_{SW}$. Therefore, it may be stated that the Alfvén wave plays an important role for the control of the field twisting at least in the deeply distant magnetotail. Also, in the case H, the result seems to coincide with the case L around the point nearby $x = -250R_J$. Here, however, $\tan\alpha$ around $x = -100R_J$ lies in the intermediate range between $r_T\Omega_0/V_A$ and $r_T\Omega_0/V_{SW}$, so that a mixing of the solar wind and the Alfvén wave propagation must determine the field structure even near the magnetotail.

3.1.2. Low Latitudinal Structure

Figures 8 and 9 display the magnetic field lines of force, which are traced from the inner boundary at the latitude 40° and 60°, nearby the day side magnetosphere in the cases H and L, respectively. In Figure 8, we can find that the magnetic field lines of force rooted at the low latitude of the inner sphere in the case L seem to be simply closed at the day side portion of the magnetosphere, and there is no great difference from the case without the rotation, i.e., similar to the Earth's magnetosphere except the spiral structure of the high latitudinal magnetic field lines of force as mentioned previously. On the other hand, in the case L, we can observe a particular structure due to the rotation. As seen in Figure 9, the low latitudinal magnetic field lines of force in the case L are trailed along the flank of the magnetosphere. And then,

the magnetic field lines of force are accumulated near the dawn side where the rotational flow collides with the solar wind. The lagging configuration of the magnetic field lines of force in the case L is consistent with the direct measurements [18,36]. The magnetic field lines of force at the dusk side, however, indicate the leading configuration since the solar wind follows the corotation of the magnetic field lines of force.

The accumulation of the magnetic field lines of force implies that the intensity of the magnetic field becomes strong at the prenoon region of the outer magnetosphere. Actually, in the case L, the southward component of the magnetic field along 0900 LT increases in the region about from $60R_J$ to $75R_J$, whereas the intensity of the magnetic field monotonically decreases and is flattened in the middle magnetosphere up to $60R_J$ (Figure 10a). This feature is also well consistent with the Jovian magnetospheric model based on Pioneer and Voyager observations along the inbound pass [1,3]. In the case H, however, the peaking in the outer magnetosphere is much weaker than the case L and the profile resembles the no rotational case. In the afternoon region, on the other hand, the rise of the intensity of the magnetic field is hardly observed near the magnetopause in either case as found in Figure 10b. Especially, in the case L, the profile of the magnetic intensity forms plateau farther than $50R_J$ like as the middle magnetosphere in the prenoon region. Thus, the dawn-dusk asymmetry for the distribution of the magnetic field at the low latitude arises from the fact that the solar wind promotes a lagging and a leading of the magnetic field lines of force at the dawn and at the dusk, respectively.

Also, with respect to the environment of the plasmas, we can find the remarkable feature originated from the rotation at the low latitudinal magnetosphere. As shown in Figure 11, it is observed that the plasma disc, which corresponds to the crescent in Figure 3, is formed in the case L, wherein the dawn side is wider than the dusk side. On the other hand, the evident disc-like thin structure is not formed in the case H. The reason was briefly inferred in [19] such that the internal structure of the rotating magnetosphere may be sensitively affected by the dynamic pressure of the solar wind. Here, we can clearly see the structural alteration of the rotating magnetosphere in response to the parameters of the external flow in Figures 12a and 12b, those present the plasma convection in the equatorial plane in the cases H and L, respectively. Here the red arrows indicate the region where the magnetic energy is dominant rather than the kinetic energy, while the blue arrows show the kinetic energy-dominant region. It is found at once that the magnetic energy exceeds the kinetic energy over the day side region in the case H, while the kinetic energy is dominant there in the case L. Thus, it is expected that the internal structure of the rotating magnetosphere is converted from a magnetically (dynamically) dominant system into a dynamically (magnetically) dominant system with the slow-down (speed-up) of the external flow, though the present simulations are performed only under the steady inflow condition. It suggests that the sponginess of the Jovian magnetopause could be understood as a transition between two different structures, caused by the variation of the dynamic pressure of the solar wind.

3.1.3. Cusp

The cusp structure of the Earth's magnetosphere appears in the day side high (or rather middle) latitudinal region. The Earth's magnetospheric cusp is regarded as the boundary region between the closed magnetic field lines of force on the day side magnetopause and the open magnetic field lines of force which construct a part of the magnetotail. Meanwhile, it was reported that a signature of the Jovian magnetospheric cusp may have been detected by the Ulysses observations along the outbound pass whose trajectory traversed the dusk side magnetopause with the middle latitude [6].

In Figure 2, we can see a cusp-like structure nearby the middle latitudinal afternoon region. The cusp is observed as a separated region between the day side closed magnetic field lines of

force and other streamed magnetic field lines of force. Here, we note that the magnetic field lines of force on the upper cusp are trailed by the solar wind and the rotation, and seem to be closed at the dawn flank of the magnetopause. Thus, if just the closed magnetic field lines of force are picked out of Figure 2, as shown in Figure 13, the cusp is clearly seen at the middle latitudinal zone of the afternoon region. Also, as seen in Figure 14, the cusp-like higher pressure region is constructed in the middle altitudinal magnetosphere at the dusk side. This means that, unlike the Earth's magnetosphere, the magnetic field lines of force, those form the cusp of the Jovian magnetosphere, are closed at the day side and at the dawn side magnetosphere, and are rooted to the afternoon region of the inner sphere.

Here, in order to specify the location of the cusp, the average pressure along the magnetic flux, $\langle P \rangle = \int (P/B)dl \ / \ \int (1/B)dl$, is drawn in Figures 15a and 15b for the case L, where $\langle P \rangle$ is projected on the hemispheres $r = r_0$ and $45R_J$, respectively. Since the plasma pressure in the cusp must be higher than their surroundings, we can easily find the location of the cusp with this image [37]. The zonal region with the higher pressure (i.e., the zonal whiter region in Figure 15), which must be the signature of the cusp, is located at the afternoon rather than the noon. Besides, we note that the cusp region for $r = 45R_J$ turns more counterclockwise than the case of $r = r_0$. From that, we can construct a three dimensional structure of the cusp as shown in Figure 16, where the cusp (dotted lines) is distorted right-handedly with the distance from Jupiter.

3.1.4. Plasmoid

It was observed in Figure 2 that the isolated magnetic field lines of force appears in the tail region of the magnetosphere. This structure should be called as the plasmoid, which must be formed through magnetic reconnection at the current sheet of the tail region. In our model, since the ideal MHD equations are adopted, magnetic reconnection does not take place in a strict sense. However, the numerical dissipation, which is enhanced in the TVD scheme when the gradient of the physical quantity becomes sharp, works as the effective resistivity and may trigger magnetic reconnection. The dependence of the resistivity cannot be discussed quantitatively here.

As briefly mentioned in [19], we can observe strong B_y components in the plasmoid in spite of the absence of B_y components in the IMF. This is due to the fact that the magnetic field lines of force at the tail region must be trailed by the planetary rotation, as illustrated in Figure 17. Thus, the plasmoid structure is quite different from that of the non-rotating magnetosphere like that in the Earth's magnetosphere.

Because of the trailing effect, the magnetic tension force points toward the tail-dusk side as seen in Figure 17. Therefore, in addition to the influence of the planetary rotation which directly generates the rotational flow in the equatorial plane, magnetic reconnection driven in the rotating magnetosphere must induce the novel pattern of the plasma convection at the tail. The global plasma convection in the equatorial plane are plotted with the magnetic neutral line and the magnetopause for the cases H and L in Figures 18 and 19, respectively.

In both cases, the X-type magnetic neutral line appears in the near tail, and is extended toward the distant dawn side tail. Also, the O-type neutral line appears parallel to the x axis in the dusk side tail. The plasmas at the distant tail in the case H are accelerated to the tail-dusk direction as found in [19] by the magnetic tension force indicated in Figure 17. On the other hand, as seen in Figure 19, strong positive V_y component cannot be detected in the region surrounded by the magnetic neutral line at the tail in the case L. Since, in this case, the inertia of the rotational flow is relatively important rather than in the case H, V_y component within the plasmoid becomes weaker. Apparently, the flow structure in the case L may partly resemble the cross-tail flow model proposed by *Cheng and Krimigis* [17] based on the Voyagers'

observations. Also, the flow induced by magnetic reconnection at the tail seems to correspond to the radial outflow of the conceptual model by *Vasyliunas* [16], where the topological changes of the magnetic field lines of force are taken into consideration.

3.2. Cases With IMF

It has been well known for the Earth's magnetosphere that the IMF much affects the global magnetospheric structure through magnetic reconnection. Also, the evidence for magnetic reconnection in the dayside Jovian magnetopause was presented by in-situ observations [38]. In the following, let us study the cases that the uniform magnetized external flows are applied to the inflow boundary. Particularly, in the cases N and S, the solar wind includes the northward and the southward IMF, respectively. Since the magnetic polarity of Jupiter is reversed from the polarity of Earth, the northward IMF is opposite to the magnetic field inside the Jovian magnetosphere on the equatorial plane while the southward IMF is parallel to that. Here, as mentioned previously, since the resistivity is produced by the numerical dissipation in the present model, quantitative discussions for the reconnection rate are out of the scope of this paper.

3.2.1. Interaction With Northward IMF

The IMF of the case N is anti-parallel to the magnetic field originated from Jupiter on the equatorial plane. In this system, we can infer from the knowledge of the Earth's magnetosphere, especially from the previous simulation works, that magnetic reconnection takes place at the front side of the magnetosphere since the magnetic polarities are reversed on each side of the magnetopause [39,40]. Figure 20 separately displays three classes of the magnetic field lines of force; lines rooted to the inner sphere, the IMF, and the plasmoid. It is observed that the reconnected magnetic field lines of force seem to be stretched and convected toward the tail. In order to specify the reconnection feature in the case N in detail, we examine the boundary of the root between the open and the closed magnetic field lines of force in Figure 21. Here, the magnetic field lines of force traced from the black region pass through the equatorial plane within the simulation domain. On the other hand, the white region shows the open region where the open magnetic field lines of force are started. For the Earth's magnetosphere, such black-white regions are simply separated by a latitude; the open region must be located at the high latitude no matter whether the IMF is imposed or not. On the other hand, in the case N, the closed region forms a peninsula at the noon-dusk area nearby 1200 LT to 1800 LT. The magnetic field lines of force rooted to just inside of the bay side boundary in the peninsula are connected to the dawn side equatorial plane, while those rooted to the inside of the low black region are closed at the day side magnetopause, as anticipated from the cusp structure in Figure 13. Therefore, the IMF must be reconnected with the magnetic field lines of force rooted to the white hollow region in the afternoon.

In the case N, as seen in Figure 22, magnetic reconnection at the tail induces the high speed tail-dusk flow, as well as in the case H (Figure 18). Thus, the northward IMF may play an important role for the compression of the magnetosphere, and it promotes strong magnetic reconnection at the tail. Moreover, it is interesting to note in Figure 20 that the magnetic field lines of force of the plasmoid may be reconnected to those of the IMF at the dusk flank, where the solar wind collides with the tail-dusk flow mentioned above. Indeed, it is found in Figure 22 that the magnetic neutral line at the tail is connected with the line of the magnetopause where the magnetic polarity is inverted in the case N. Thus, the IMF seems to deeply penetrate the tail of the magnetosphere. Since the grid at the distant tail, however, is relatively coarse in the present simulation, a minute discussion with highly resolved simulation may be needed in order

to confirm this phenomenon.

3.2.2. Interaction With Southward IMF

In contrast to the case of the northward IMF, it is expected from the simulations of the Earth's magnetosphere [21,39] that magnetic reconnection should occur in the upper region of the cusp in the case S. In the rotating magnetospheric system, as mentioned before, the cusp must be constructed by both the magnetic field lines of force closed on the day side magnetopause, which is the lower region of the cusp, and the lines closed on the dawn side magnetopause, which is the upper region (Figure 13). Therefore, in our model, magnetic reconnection at the upper region of the cusp must tear off the magnetic field lines of force on the dawn side magnetopause. Figure 23 shows the global configuration of the magnetic field lines of force, where the magnetic field lines of force rooted to the inner sphere and the isolated lines are separately displayed as in Figure 20. We can find that magnetic reconnection peels off the magnetic field lines of force on the upper region of the dawn side magnetopause, and as a result, the dawn side magnetosphere relatively shrinks.

While the plasmoid in the tail region appears also in the case S, magnetic reconnection at the tail may be weakened compared to any other cases, so that the size of the plasmoid is smaller than the other cases. Thus, as seen in Figure 24, the anti-corotational flow induced by magnetic reconnection is not observed, and the plasmas almost flow across the tail. This flow structure at the tail is apparently similar to the flow in the case L (Figure 19) rather than in the cases H and N (Figures 18, 22), while the size of the dawn side magnetosphere in the case S is fairly narrower than in the case L.

4. Discussion

4.1. Global Model

Based on the results of the present simulations, we propose a global model of the Jovian magnetosphere. Figure 25 shows the schematic diagram of the Jovian magnetospheric structure without the IMF, where the magnetic field lines of force on the magnetopause viewed from the noon, the north, and the prenoon-north are drawn in Figures 25a, 25b, and 25c, respectively. Here, thick solid lines indicate the magnetopause and the cusp, and thin solid lines with arrows and chain-dotted line show the magnetic field lines of force and the equatorial plane, respectively. Besides, the model of the large scale plasma convection in the equatorial plane with the X- and the O-type magnetic neutral line is illustrated in Figure 25d.

We infer that the magnetic field lines of force colored by red are accumulated at the prenoon red-shaded region, where the plasma flow is almost stagnant since the rotational flow collides with the solar wind. Therefore, the dynamic pressure of the rotational flow in the dawn side spreads out the magnetopause against the dynamic pressure of the solar wind and the size of the magnetosphere is expanded to the dawn side rather than the dusk side. Actually, the ascendance of the intensity of the magnetic field caused by the flux piling up is observed at the prenoon region, as measured in-situ observations (e.g., [1,3]). In this prenoon region, while the Kelvin-Helmholtz (K-H) instability is believed to cause the prenoon turbulence according to the Voyager-based conceptual model by *Cheng and Krimigis* [17], our calculation cannot resolve a fine structure related to the K-H vortices. The plasmas at the noon region shaded by blue are accelerated by the magnetic tension force and the solar wind, those release the stress of the accumulated magnetic field lines of force. Therefore, the intensity of the magnetic field is flattened at the afternoon region in contrast with the prenoon region. The rotational speed at this blue-shaded region is accelerated up to about the rigid corotational speed with Jupiter, i.e.,

about twice larger than $r\Omega_0$. This process is observed not only in the case H, which is the same case as shown in [19], but also in the case L (not shown here). It is well consistent with the results analyzed from in-situ observations [41-43], which could not be explained by the rotating magnetospheric model without the interaction of the solar wind [11].

At the dawn flank shaded by green, on the other hand, the magnetic field lines of force are carried toward the tail by the tailward flow which may correspond to the magnetospheric wind as presented by *Krimigis et al.* [9]. In our model, the magnetic field lines of force on the dawn flank magnetopause are connected to the upper region of the cusp through the high altitudinal magnetopause as illustrated by the green lines in Figure 25. Since the plasmas at the cusp must rotate counterclockwise in the view from the north as in Figure 25b, the plasmas on the green lines totally flow toward the tail. Therefore, the plasmas in the high altitudinal magnetosphere, those are frozen-in the green lines, must flow toward the tail, and makes an anti-corotational flow.

Figure 26a shows the velocity perpendicular to the magnetic field, $V_\perp$, (i.e., the frozen-in motion) on $x = 0$ plane viewed from the noon in the case L, where the blue and the red vectors indicate the sunward and the anti-sunward flow, respectively. We find at once that the perpendicular flow indicates the corotation in the dusk side magnetosphere. On the other hand, in the dawn side magnetosphere, the perpendicular flow at the high altitude includes the tailward component, which indicates an anti-corotational sense. In addition to the perpendicular flow, the field-aligned flow may be induced by the centrifugal force. After all, the entire plasma flow on $x = 0$ plane is shown in Figure 26b, where the solar wind components are also included. It is eventually found that the anti-corotational flow appears also in the middle altitudinal dawn magnetosphere. This is due to that the centrifugal force accelerates the field-aligned flow in the middle altitudinal dawn magnetosphere, where the magnetic field lines of force have the lagging configuration with a strong x component. Thus, it may be natural that the anti-corotational flows, which might be detected by the Ulysses observations along the prenoon inbound pass [44,45], are generated at the middle and the high altitudinal dawn in the Jovian magnetospheric system. According to the present model, the inbound flybys of the Pioneers, the Voyagers, and the Ulysses might pass through one of the most characteristic regions in the Jovian magnetosphere specified by blue, red, and green in Figure 25, those locations are sensitively varied by the condition how compressed the magnetosphere is.

4.2. Tail Reconnection

As discussed above, the magnetic field lines of force at the middle or the low altitudinal tail forms the lagging configuration. Therefore, at the tail region of the Jovian magnetosphere, magnetic reconnection must take place in the lagging magnetic field lines of force as illustrated in Figure 17. Magnetic reconnection for the Jovian magnetosphere has been discussed by several global models [16,18]. In these models, the edge of the X-line is believed to touch on the dawn side magnetopause, so that the magnetospheric wind at the dawn flank observed by Voyager [9] is considered to be the reconnection-induced flow. Our model, however, does not show such a structure, but the magnetic neutral line at the dawn side is distributed parallel to the sun-Jupiter line, as shown in Figure 25d.

Also, another global model by an MHD simulation clearly indicated the evidence of magnetic reconnection at the tail [20]. In that model, the dawn side edge of the magnetic neutral line seems to be also separated from the dawn side magnetopause. However, in our model, the flow induced by magnetic reconnection turns toward the tail-dusk side in the deeply distant tail, especially for the case of the highly compressed magnetosphere, whereas the model by *Ogino et al.* [20] did not indicate the tail-dusk flow. The difference between these two models may arise from the difference of the inner or the middle magnetospheric state. Indeed, the global

plasma convection for the case L (Figure 19), which is dynamically dominant system as seen in Figure 12, is quite similar to the pattern of the large scale flow as found in Plate 2 of [20]. It is suspected that the magnetic tension force in these cases is too weak to reverse the rotational flow completely within the simulation domain.

Recently, based on the Galileo observations, *Krupp et al.* [10] suggested the existence of the radial outflow bursts at the premidnight-predawn region which was thought as the different events from the magnetospheric wind in the boundary layer observed by the Voyager 2 [9]. The outflow bursts appeared closer to the planet than the magnetospheric wind. It was supposed that the bursts might be caused by the dynamic re-configurations of the Jovian magnetotail like in geomagnetic substorms [10]. Our results also show that the re-configurations of the magnetic field lines of force at the tail region happen through magnetic reconnection. These results suggest that the different types of the outward flows, the outflow bursts induced by reconnection and the magnetospheric wind, may exist in the Jovian magnetosphere.

4.3. Reconnection with IMF

Next, we present the Jovian magnetospheric model in consideration for magnetic reconnection with the northward/southward IMF. Indeed, based on in-situ observations, *Walker and Russell* [38] showed the evidence for the flux transfer event (FTE). Figures 27a and 27b show the conceptual illustrations of the cross section of the magnetic field lines of force on $x = 0$ plane in the cases of the northward and the southward IMF, respectively. Here, the lines with arrows indicate the magnetic field lines of force in both the Jovian magnetosphere and the solar wind while the dotted line sketches the magnetopause. As seen in Figure 27a, the northward IMF reconnects with the magnetic field lines of force rooted to the afternoon inner sphere, those are closed on the day side and the dusk side magnetopause. Subsequently, the reconnected magnetic field lines of force are transferred toward the tail and the magnetosphere is highly compressed by the solar wind. Therefore, the strong tail-dusk flow is induced by strong magnetic reconnection at the distant tail region as seen in Figure 22. It is much similar to the state formed by the strong solar wind (Figure 18).

On the other hand, as shown in Figure 27b, magnetic reconnection with the southward IMF takes place in the upper region of the cusp, and tears off the magnetic field lines of force on the dawn side magnetopause which correspond to the green lines in Figure 25. Therefore, the size of the dawn side magnetosphere shrinks and subsequent magnetic reconnection in the tail must be weakened. As found from Figures 24 and 19, the reconnection-induced flow in the cases L and S hardly has the duskward component, in contrast with the cases H and N as seen in Figures 18 and 22. Thus, the east-west asymmetry in the Jovian magnetosphere must greatly depend on not only the dynamic pressure of the solar wind but also the polarity of the IMF.

5. Summary

We have performed the three dimensional MHD simulation of the interaction between the rotating magnetosphere and the high speed external flow with and without the IMF in order to investigate the global structure of the Jovian magnetosphere. Our results showed that the magnetic field lines of force near the pole are highly twisted, in which the pitch angle of the helical magnetic field lines of force seems to be determined by the ratio of the corotational speed and the local Alfvén speed in the deeply distant magnetotail. Therefore, the distant magnetotail structure may be almost independent of the speed of the solar wind. On the other hand, the magnetospheric structure at the low altitude was fairly controlled by the dynamic pressure of the solar wind. The magnetic field lines of force were accumulated at the prenoon region due to the lagging of the corotation, and therefore, the strength of the magnetic field rose up especially

in the case L. At the dusk side, however, the intensity of the magnetic field from the middle to the outer magnetosphere was flattened since there is no obstacle to pile the magnetic field lines of force.

Also we indicated that the global plasma convection is largely affected not only by the planetary rotation but also by the solar wind. In the tail region, the corotational flow was broken by the tailward flow induced by magnetic reconnection. Particularly, in the case H, the tail-dusk flow was generated via strong magnetic reconnection at the tail region, while such a flow structure was not observed in the case L. In the case including the uniform northward IMF, the magnetic field lines of force rooted to the afternoon inner sphere are subject to reconnection at the day side magnetopause. On the other hand, magnetic reconnection with the southward IMF occurs in the upper regions of the cusp and tears off the magnetic field lines of force on the dawn side magnetopause. As a result, the dawn side magnetopause relatively shrinks. In this case, magnetic reconnection and the flow related to reconnection at the tail were partially suppressed, while the northward IMF extremely promoted tail reconnection. Thus, for the large scale pattern of the plasma convection in the Jovian magnetosphere, reconnection must play a crucial role.

Here, we discussed only the quasi-steady structure of the global Jovian magnetosphere, and the dynamical feature will be presented elsewhere. Also, in order to treat the tilting effect of the magnetic dipole axis from the rotation axis, we must develop the fully three dimensional MHD simulation without any symmetries.

Acknowledgment

References

1. Acuña, M. H., K. W. Behannon, and J. E. P. Connerney, in *Physics of the Jovian Magnetosphere,* edited by A. J. Dessler, p. 1, Cambridge Univ. Press, N. Y. (1983).

2. Belcher, J. W., in *Physics of the Jovian Magnetosphere,* edited by A. J. Dessler, p. 68, Cambridge Univ. Press, N. Y. (1983).

3. Smith, E. J., R. W. Fillius, and J. H. Wolf, *J. Geophys. Res.,* **83**, 4733 (1978).

4. Lepping, R. P., L. F. Burlaga, and L. W. Klein, *Geophys. Res. Lett.,* **8**, 99 (1981).

5. Smith, E. J., K.-P. Wenzel, and D. E. Page, *Science,* **275**, 1503 (1992).

6. Bame, S. J., B. L. Barraclough, W. C. Feldman, G. R. Gisler, J. T. Gosling, D. J. McComas, J. L. Phillips, M. F. Thomsen, B. E. Goldstein, and M. Neugebauer, *Science,* **257**, 1539 (1992).

7. Vasyliunas, V. M., L. A. Frank, K. L. Ackerson, and W. R. Paterson, *Geophys. Res. Lett.,* **24**, 869 (1997).

8. Woch, J., N. Krupp, A. Lagg, B. Wilken, S. Livi, and D. J. Williams, *Geophys. Res. Lett.,* **25**, 1253 (1998).

9. Krimigis, S. M., T. P. Armstrong, W. I. Axford, C. O. Bostrom, C. Y. Fan, G. Gloeckler, D. C. Hamilton, and R. D. Zwickl, *Geophys. Res. Lett.,* **7**, 13 (1980).

10. Krupp, N., J. Woch, A. Lagg, B. Wilken, S. Livi, and D. J. Williams, *Geophys. Res. Lett.,* **25**, 1249 (1998).

11. Hill, T. W., *J. Geophys. Res.*, **84**, 6554 (1979).

12. Yang, Y. S., R. A. Wolf, R. W. Spiro, T. W. Hill, and A. J. Dessler, *J. Geophys. Res.*, **99**, 8755 (1994).

13. McNutt, R. L., Jr., J. W. Belcher, J. D. Sullivan, F. Bagenal, and H. S. Bridge, *Nature*, **280**, 803 (1979).

14. Brice, N. M., and G. A. Ioannidis, *Icarus*, **13**, 173 (1970).

15. Kennel, C. F., and F. V. Coroniti, *Ann. Rev. Astron. Astrophys.*, **15**, 389 (1977).

16. Vasyliunas, V. M., in *Physics of the Jovian Magnetosphere*, edited by A. J. Dessler, p. 395, Cambridge Univ. Press, N. Y. (1983).

17. Cheng, A. F., and S. M. Krimigis, *J. Geophys. Res.*, **94**, 12003 (1989).

18. Cowley, S. W. H., A. Balogh, M. K. Dougherty, M. W. Dunlop, T. M. Edwards, R. J. Forsyth, R. J. Hynds, N. F. Laxton, and K. Staines, *J. Geophys. Res.*, **101**, 15197 (1996).

19. Miyoshi, T., and K. Kusano, *Geophys. Res. Lett.*, **24**, 2627 (1997).

20. Ogino, T., R. J. Walker, and M. G. Kivelson, *J. Geophys. Res.*, **103**, 225 (1998).

21. Ogino, T., R. J. Walker, and M. Ashour-Abdalla, *J. Geophys. Res.*, **99**, 11027 (1994).

22. Tanaka, T., *J. Comput. Phys.*, **111**, 381 (1994).

23. Tanaka, T., *J. Geophys. Res.*, **100**, 12057 (1995).

24. Brio, M., and C. C. Wu, *J. Comput. Phys.*, **75**, 400 (1988).

25. Schmidt-Voigt, M., *Astron. Astrophys.*, **210**, 433 (1989).

26. Powell, K., G., *ICASE Rep. 94-24, CR-194902* Inst. for Comp. Appl. in Sci. and Eng., NASA Langley Res. Center, Langley, Va. (1994).

27. Gombosi, T. I., K. G. Powell, and D. L. De Zeeuw, *J. Geophys. Res.*, **99**, 21525 (1994).

28. Gombosi, T. I., D. L. De Zeeuw, R. M. Häberli, and K. G. Powell, *J. Geophys. Res.*, **101**, 15233 (1996).

29. Hirsch, C., *Numerical Computation of Internal and External Flows, Volume 2: Computational Methods for Inviscid and Viscous Flows*, John Wiley & Sons Ltd., England (1990).

30. Siscoe, G. L., and D. Summers, *J. Geophys. Res.*, **86**, 8471 (1981).

31. Hill, T. W., A. J. Dessler, and C. K. Goertz, in *Physics of the Jovian Magnetosphere*, edited by A. J. Dessler, p. 353, Cambridge Univ. Press, N. Y. (1983).

32. Krimigis, S. M., and E. C. Roelof, in *Physics of the Jovian Magnetosphere*, edited by A. J. Dessler, p. 106, Cambridge Univ. Press, N. Y. (1983).

33. Watanabe, K., and T. Sato, *J. Geophys. Res.*, **95**, 75 (1990).

34. Dessler, A. J., and R. D. Juday, *Planet. Space Sci.*, **13**, 63 (1965).

35. Isbell, J., A. J. Dessler, and J. H. Waite, Jr., *J. Geophys. Res.*, **89**, 10716 (1984).

36. Behannon, K. W., L. F. Burlaga, and N. F. Ness, *J. Geophys. Res.*, **86**, 8385 (1981).

37. Ogino, T., *J. Geophys. Res.*, **91**, 6791 (1986).

38. Walker, R. J., and C. T. Russell, *J. Geophys. Res.*, **90**, 7397 (1985).

39. Usadi, A., A. Kageyama, K. Watanabe, and T. Sato, *J. Geophys. Res.*, **98**, 7503 (1993).

40. Walker, R. J., T. Ogino, J. Raeder and M. Ashour-Abdalla, *J. Geophys. Res.*, **98**, 17235 (1993).

41. Carbary, J. F., S. M. Krimigis, E. P. Keath, G. Gloekler, W. I. Axford, and T. P. Armstrong, *J. Geophys. Res.*, **86**, 8285 (1981).

42. Kane, M., B. H. Mauk, E. P. Keath, and S. M. Krimigis, *Geophys. Res. Lett.*, **19**, 1435 (1992).

43. Kane, M., B. H. Mauk, E. P. Keath, and S. M. Krimigis, *J. Geophys. Res.*, **100**, 19473 (1995).

44. Phillips, J. L., S. J. Bame, B. L. Barraclough, D. J. McComas, R. J. Forsyth, P. Canu, and P. J. Kellogg, *Planet. Space Sci.*, **41**, 877 (1993).

45. Staines, K., A. Balogh, S. W. H. Cowley, T. M. Edwards, R. J. Forsyth, and R. J. Hynds, *Planet. Space Sci.*, **41**, 931 (1993).

Table 1: Boundary conditions in four different simulation runs.

Case	$n_{SW}(/\text{cm}^3)$	$V_{xSW}(\text{km/s})$	$B_{zSW}(\text{nT})$	$T_{SW}(\text{K})$	M_A	M_S
L	0.1	−300	0	4×10^4	∞	12.8
H	0.1	−400	0	4×10^4	∞	17.1
N	0.1	−300	1	4×10^4	4.3	12.8
S	0.1	−300	−1	4×10^4	4.3	12.8

(a)   (b)
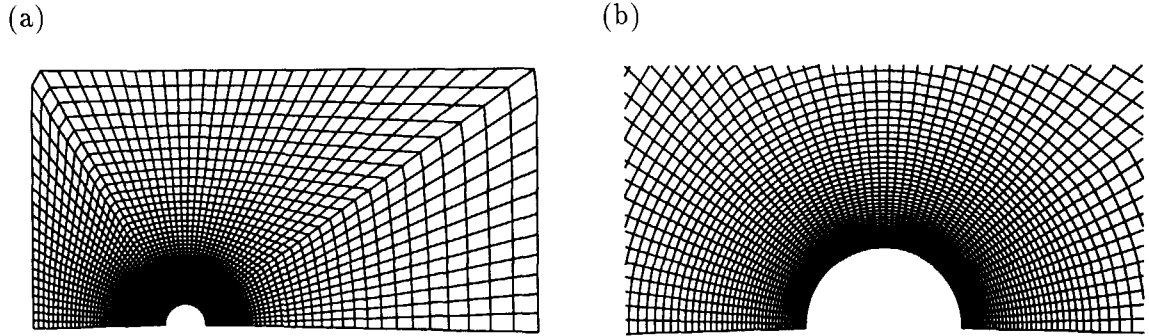
Figure 1: (a) The whole and (b) the inner grid structure of the present simulation on the x-z meridian plane. The grid structure is based on the spherical coordinate system in the inner region and is stretched in the outer region to fit the vertical wall at the front boundary.

This is a blank page.
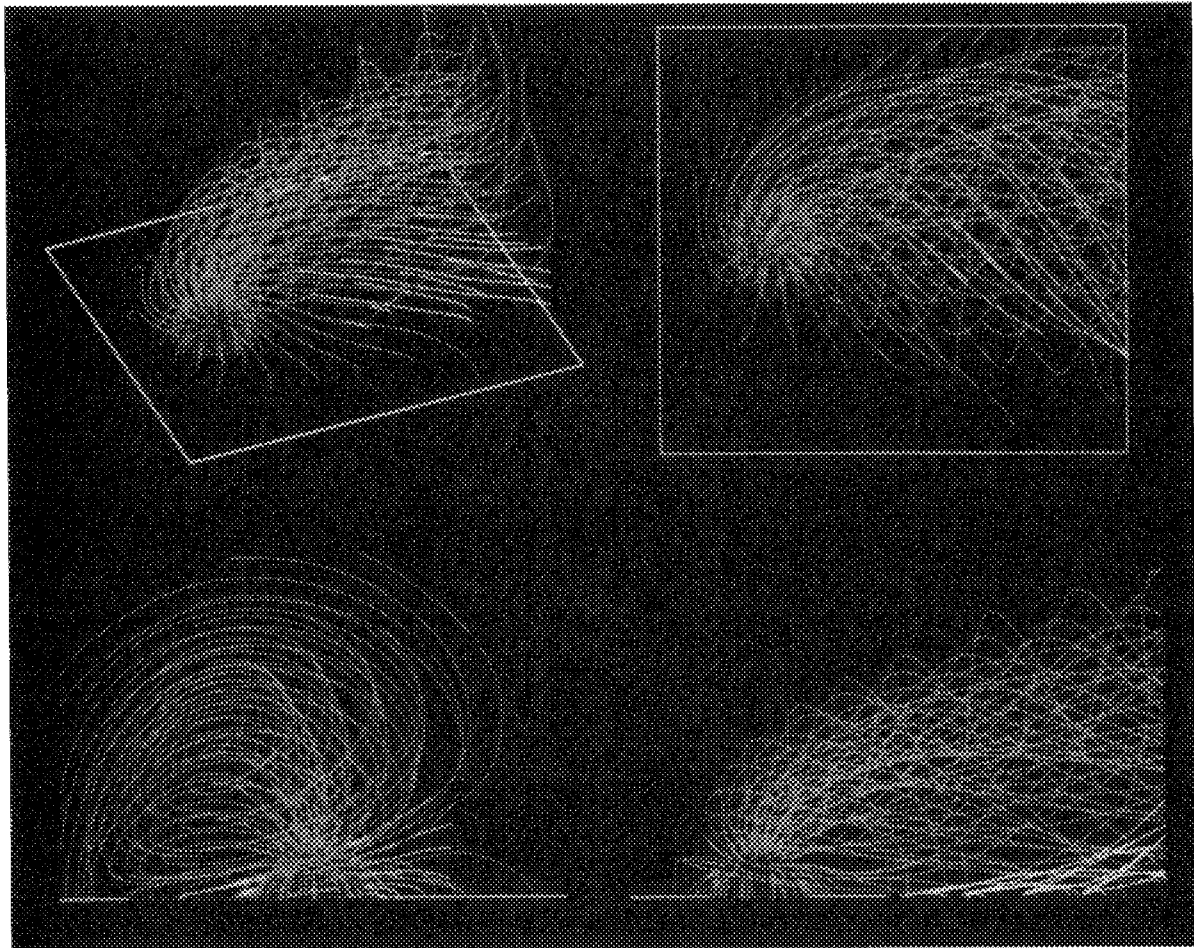
Figure 2: Three dimensional structure of the magnetic field lines of force in the case L, where the green lines are rooted to the inner sphere and the yellow lines indicate the isolated lines from the planetary boundary. The purple line on the equatorial plane shows the magnetic neutral line. The top-left, the top-right, the bottom-left, and the bottom-right panels are the view from the afternoon-north, the north, the noon, and the dusk, respectively.

This is a blank page.
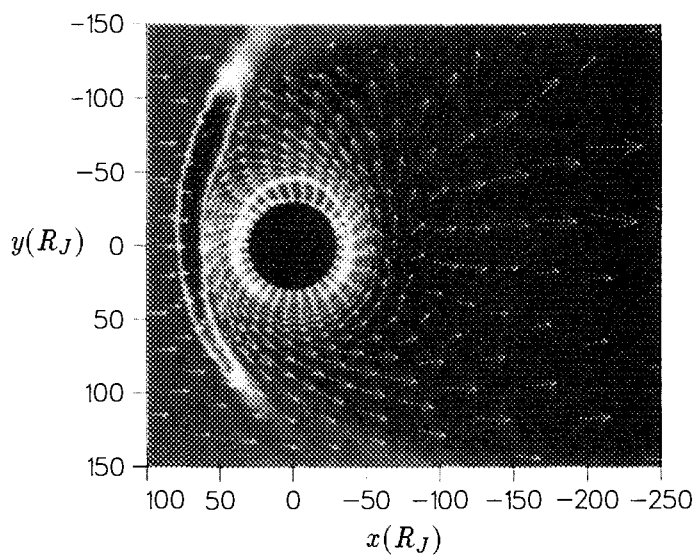
Figure 3: The vectors of the plasma flow and the density contour on the equatorial plane in the case L, where the purple line shows the magnetic neutral line. Redder regions indicate higher density regions (red regions are more than $0.5/\text{cm}^3$) while bluer regions are lower.

This is a blank page.
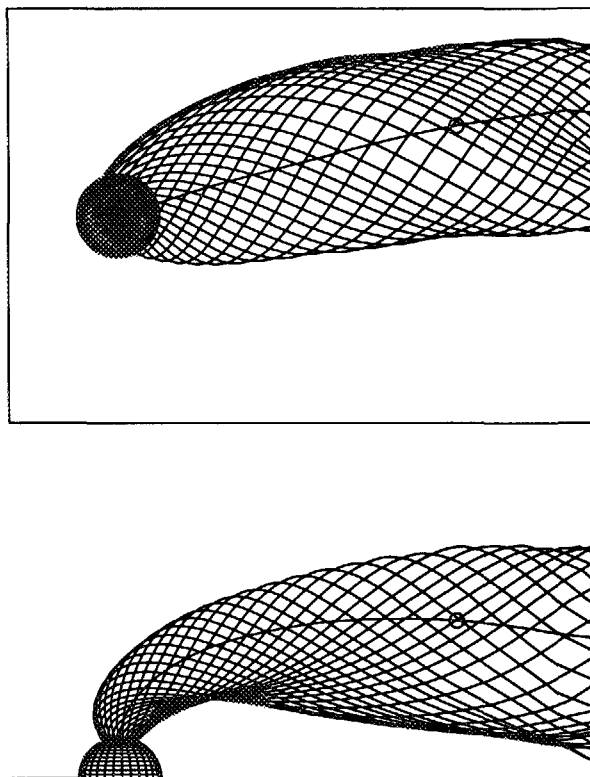
Figure 4: The spiral structure of the typical magnetic field lines of force rooted to the high latitude ($\theta = 60°$, $90°$) in the case L viewed from the north (top) and from the dusk (bottom). The circle indicates the point $(-250 R_J, -30 R_J, 110 R_J)$.
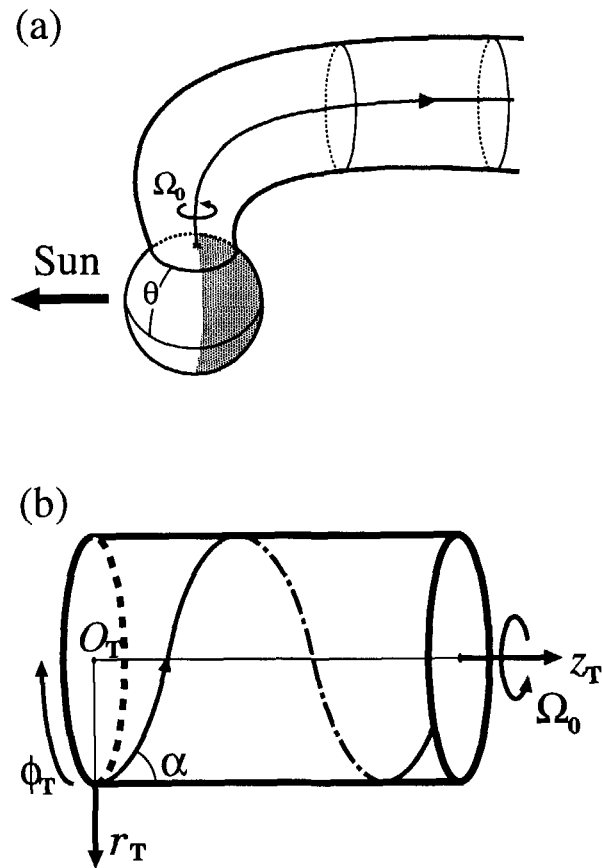
Figure 5: (a) Schematic diagram of the high latitudinal magnetic field lines of force, where the flux surface and the magnetic axis are formed. (b) The coordinate system to analyze the spiral magnetic field lines of force, where α denotes the pitch angle of the lines.

(a) (b)
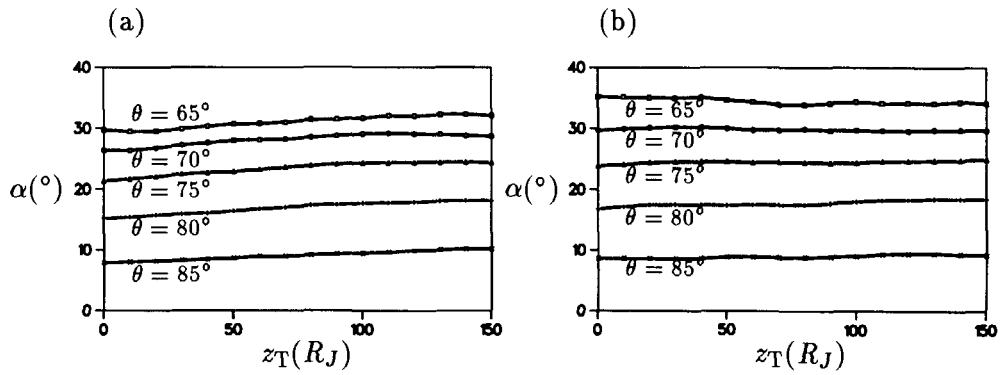
Figure 6: The average pitch angles α with respect to z_T specified by some latitudes θ ($\theta = 65°$, 70°, 75°, 80°, 85°) in (a) the case H and (b) the case L.
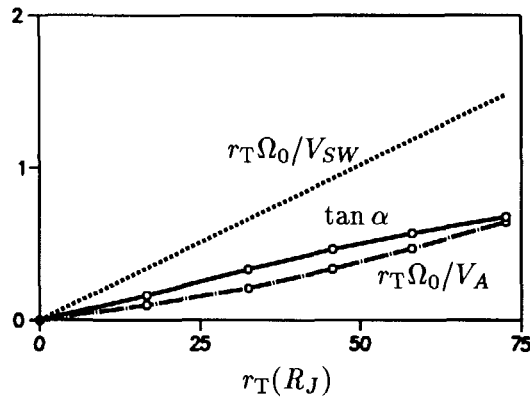
Figure 7: The average ratio of B_{θ_T} to B_{z_T} on the flux surface, i.e. $\tan \alpha$, is plotted as a function of the average radius r_T of the magnetotail for the case L around ($-250R_J, -30R_J, 110R_J$), which is marked by circle in Figure 2. Also, $r_T \Omega_0 / V_{SW}$ and $r_T \Omega_0 / V_A$ are plotted by the dotted line and the chain-dotted line with circles, respectively.
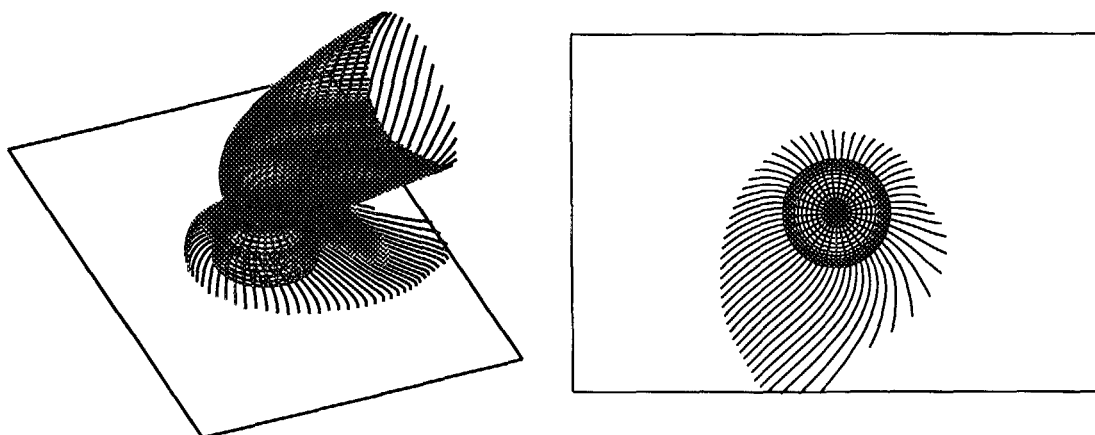
Figure 8: The magnetic field lines of force in the case H, those are traced from $\theta = 40°$ and $60°$. The left and right panels are the view from the afternoon-north and the north, respectively.
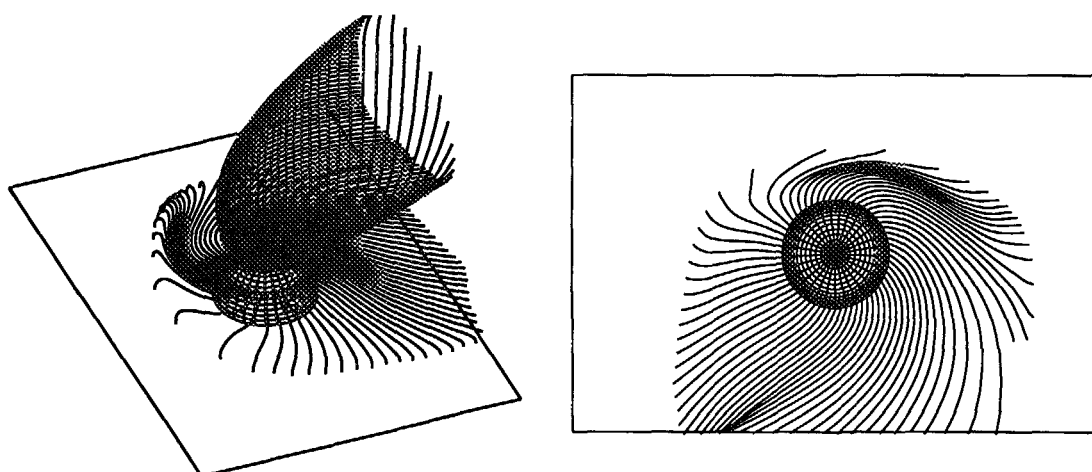
Figure 9: The same as Figure 8 in the case L.

(a)

$B_z(\mathrm{nT})$

case L

case H

no rotation
($V_{SW} = 300\mathrm{km/s}$)

$r(R_J)$

(b)

$B_z(\mathrm{nT})$

case H

case L

no rotation
($V_{SW} = 300\mathrm{km/s}$)

$r(R_J)$
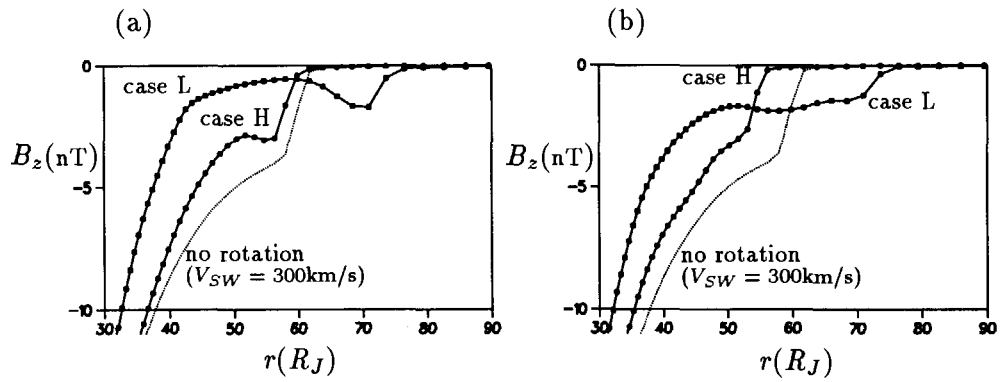
Figure 10: The z component of the magnetic field B_z on the equatorial plane in the cases H and L is plotted as a function of the radial distance (a) along the prenoon (0900 LT) and (b) along the afternoon (1500 LT) pass, respectively. The dotted line shows the result in the non-rotating case with $V_{xSW} = -300\mathrm{km/s}$ for the sake of comparison.

This is a blank page.
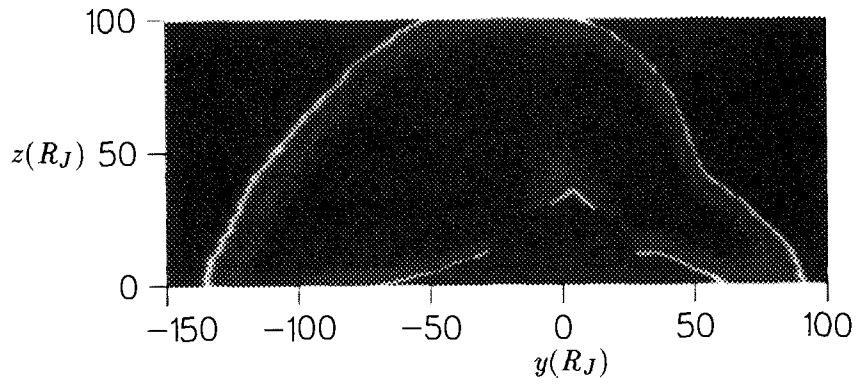
Figure 11: The contour of the density on $x = 0$ meridian plane in the case L. Redder regions indicate higher density regions (red regions are more than $0.1/\text{cm}^3$) while bluer regions are lower.

This is a blank page.
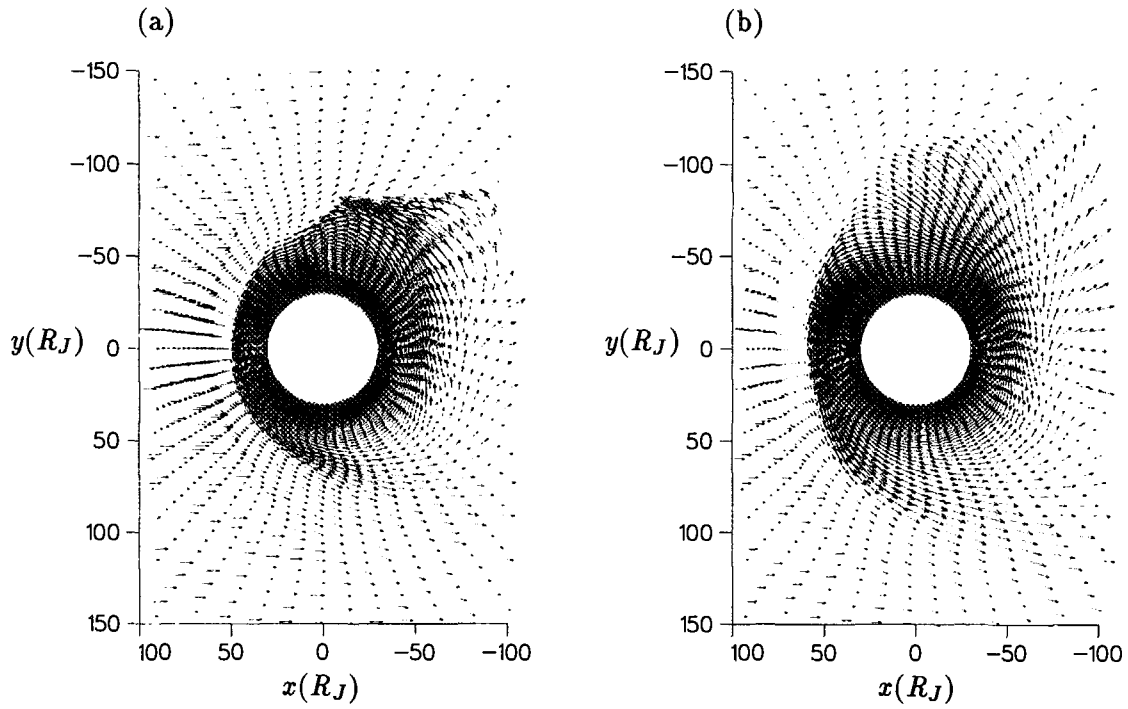
Figure 12: The vectors of the plasma flow on the equatorial plane (a) in the case H and (b) the case L, respectively. Here, the blue and red arrows indicate the magnetic energy-dominant region and the kinetic energy-dominant region, respectively.

This is a blank page.
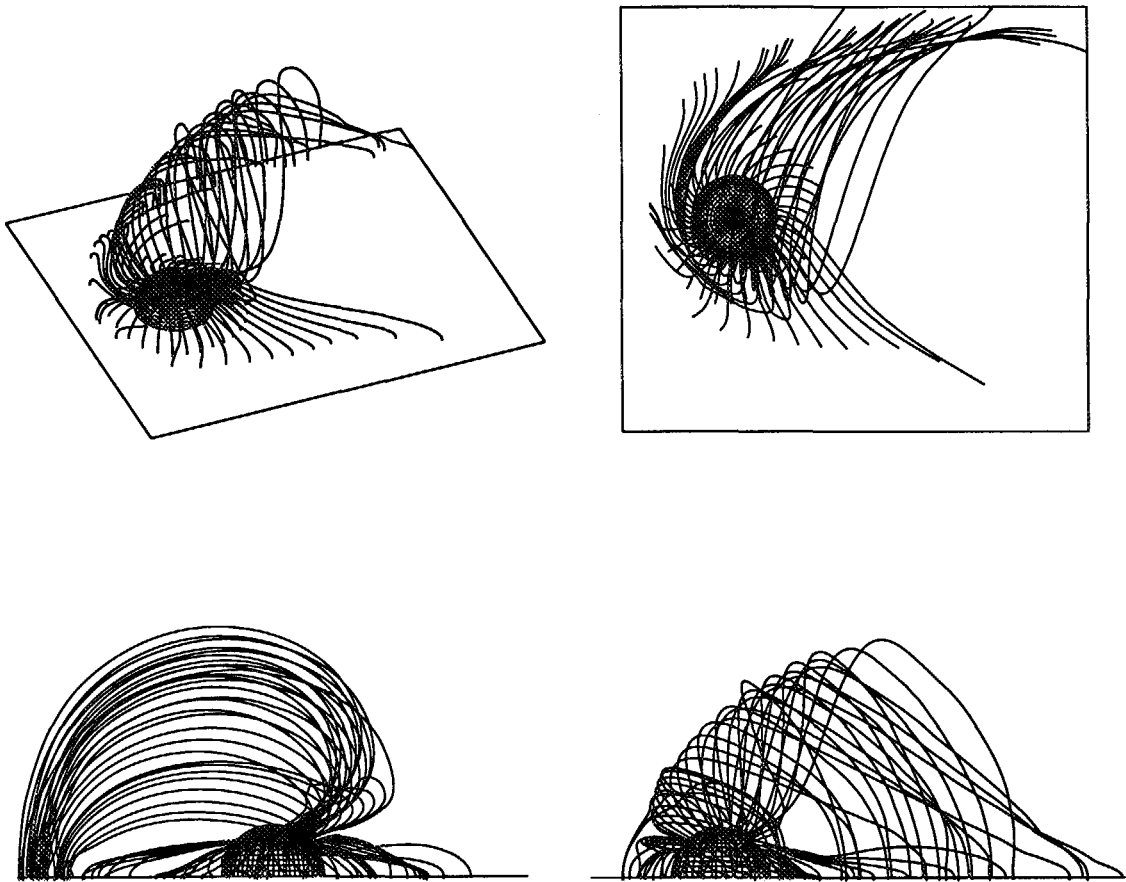
Figure 13: The closed magnetic field lines of force, which pass through the equatorial plane, are picked out from the green lines in Figure 2. The top-left, the top-right, the bottom-left, and the bottom-right panels are viewed from the afternoon-north, the north, the noon, and the dusk, respectively.
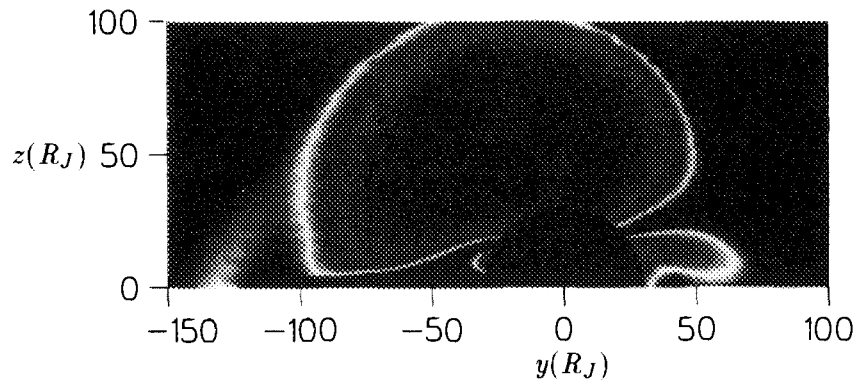
This is a blank page.

Figure 14: The contour of the pressure on $x = 0$ meridian plane in the case L. Redder regions indicate higher pressure regions (red regions are more than 3.3×10^{-11}erg/cm^3) while bluer regions are lower.

This is a blank page.

(a)

(b)
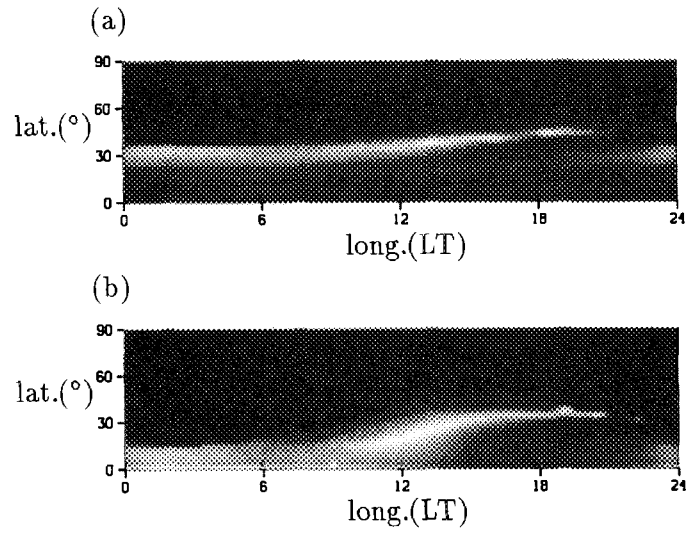
Figure 15: Gray scale images of the average pressure along the magnetic field lines of force is mapped onto the hemisphere of the radius (a) $r_{\bar{P}_B} = r_0$, and (b) $45R_J$ in the case L. The ordinate and the abscissa indicate the latitude measured by a degree and the longitudinal local time, respectively. Whiter regions indicate higher pressure.
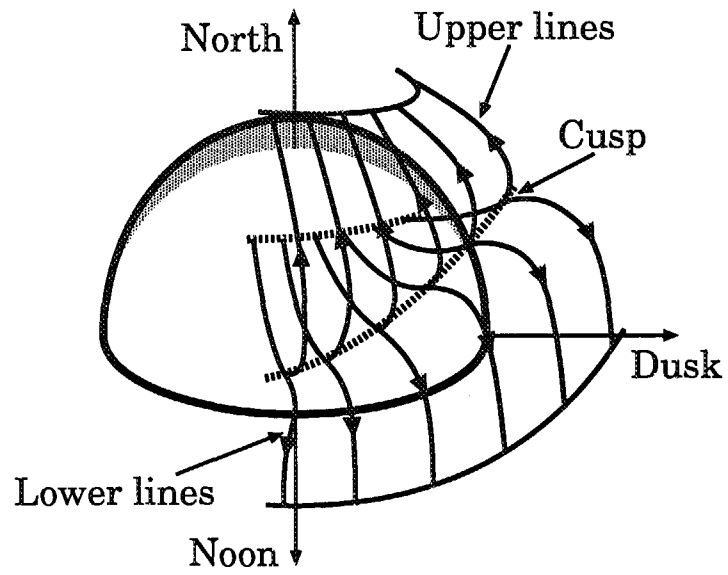
Figure 16: Three dimensional view of the cusp of the Jovian magnetosphere. Here, the inclined dotted lines depict the twisted structure of the cusp.
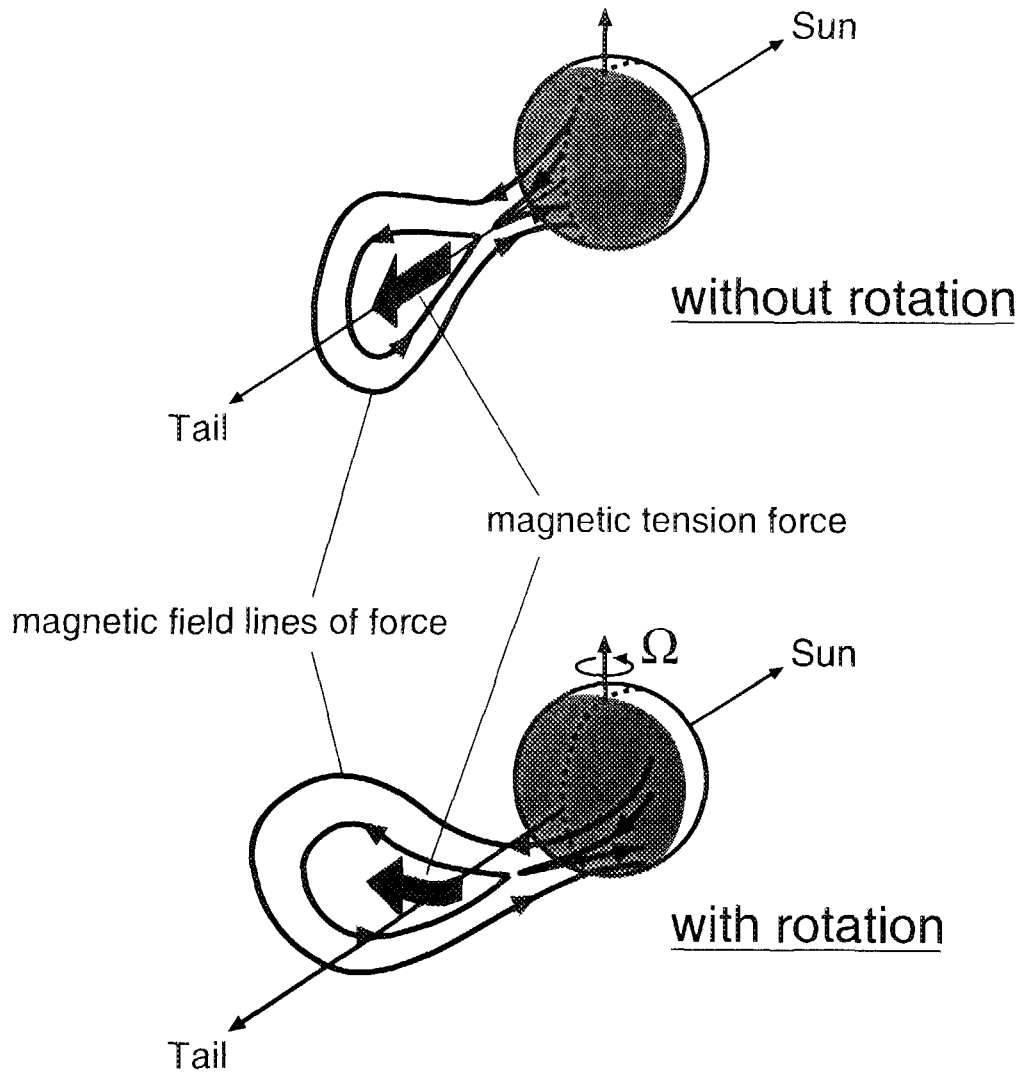
Figure 17: The illustration of the plasmoid configuration and the tension force on it produced by tail reconnection in the cases without and with the rotation.
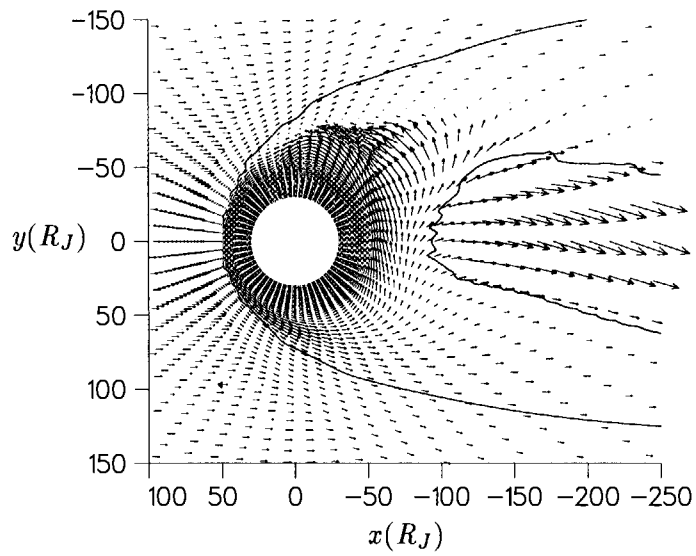
Figure 18: The vectors of the plasma flow on the equatorial plane in the case H, where the solid line shows the magnetopause and the magnetic neutral line.
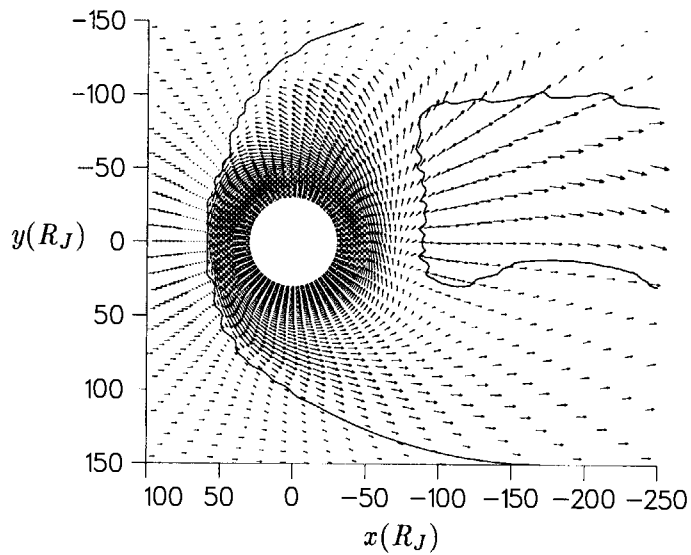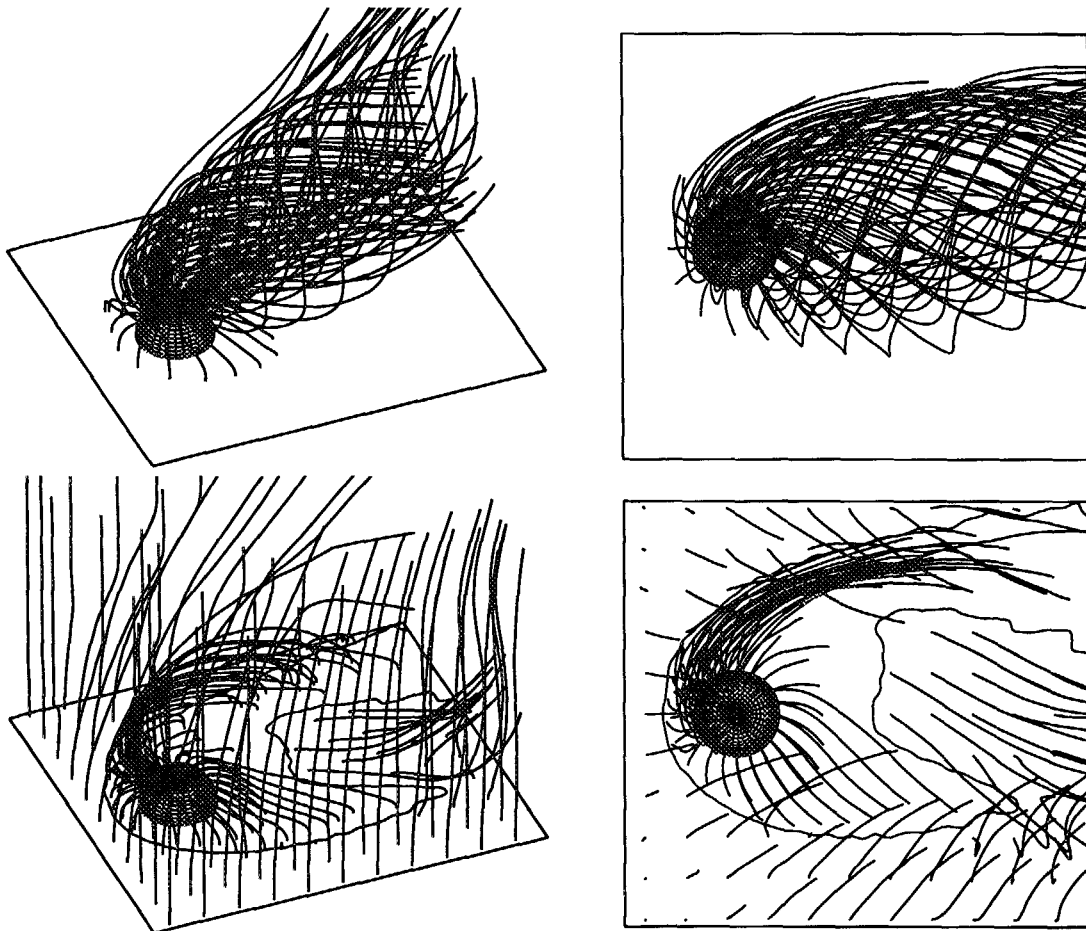

Figure 19: The same as Figure 18 in the case L.

Figure 20: Three dimensional structure of the magnetic field lines of force in the case N. The top-left and the top-right panels show the magnetic field lines of force rooted to the inner sphere viewed from the afternoon-north and from the north, respectively. The bottom-left and the bottom-right indicate the IMF, the closed lines within the domain, and the plasmoid, viewed from the afternoon-north and from the north, respectively.
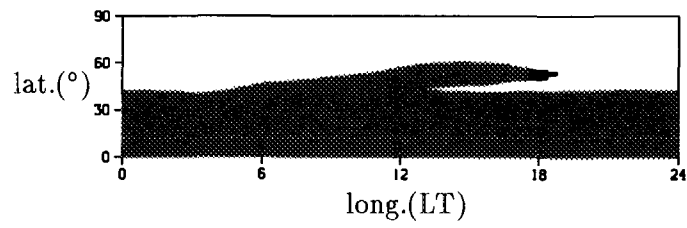
Figure 21: The black-white image on the inner sphere where the white and the black regions show the roots of the closed and the open magnetic field lines of force, respectively. The ordinate and the abscissa indicate the latitude measured by a degree and the longitude by a local time, respectively.
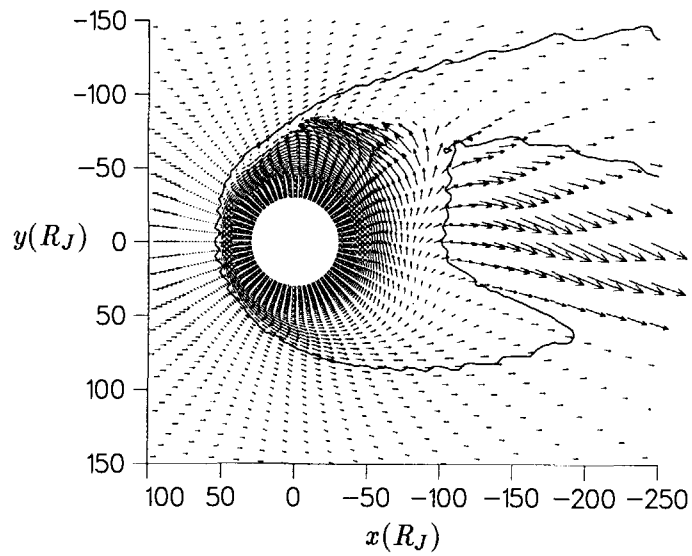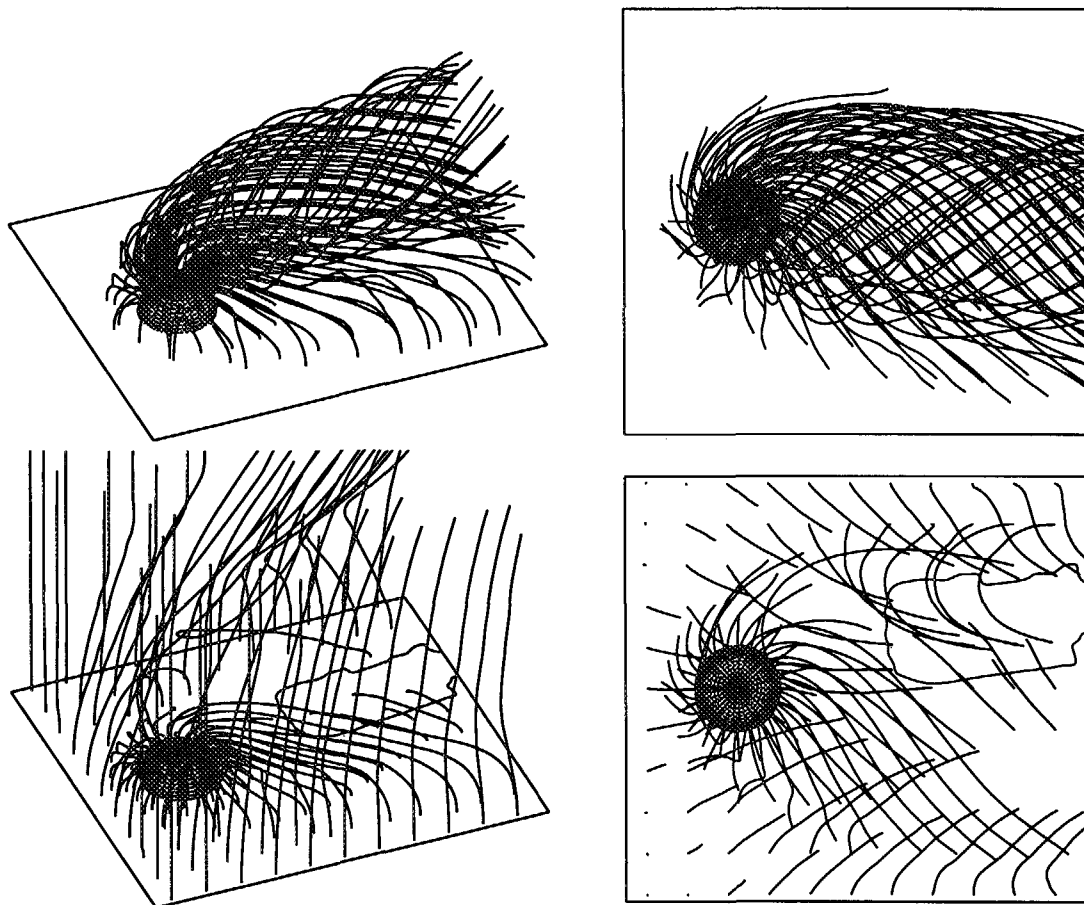

Figure 22: The same as Figure 18 in the case N.
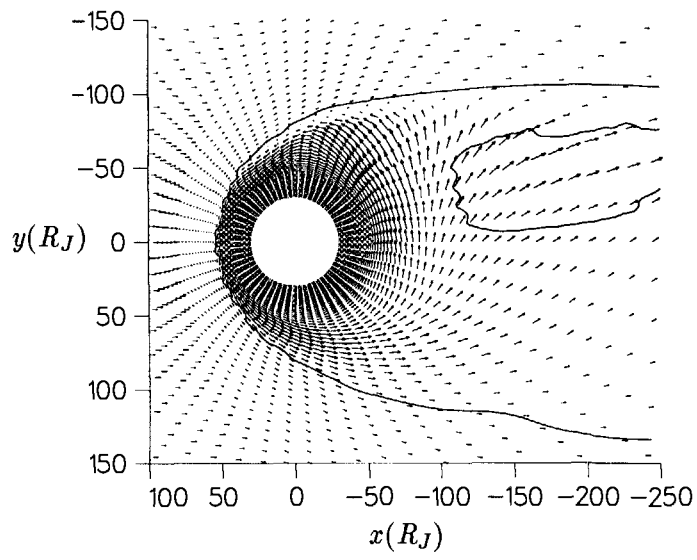
Figure 23: The same as Figure 20 in the case S.

Figure 24: The same as Figure 18 in the case S.
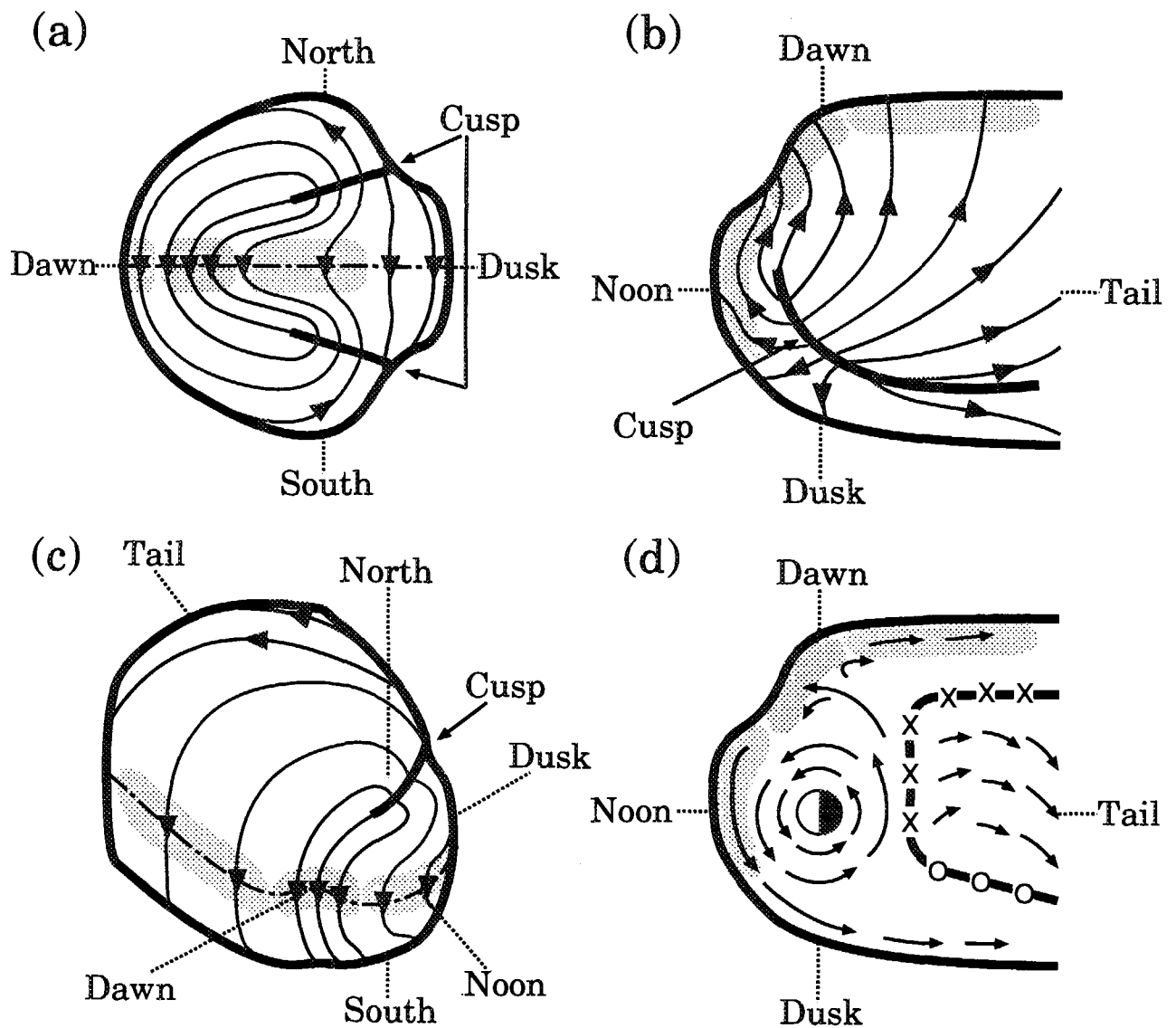
(a)

(b)

(c)

(d)

Figure 25: The schematic diagram of the Jovian magnetospheric model without the IMF. The magnetic field lines of force on the magnetopause viewed from (a) the noon, (b) the north, and (c) the prenoon-north are drawn. Also, the global plasma convection in the equatorial plane is illustrated in (d). The meanings of blue, red, and green are stated in the text.
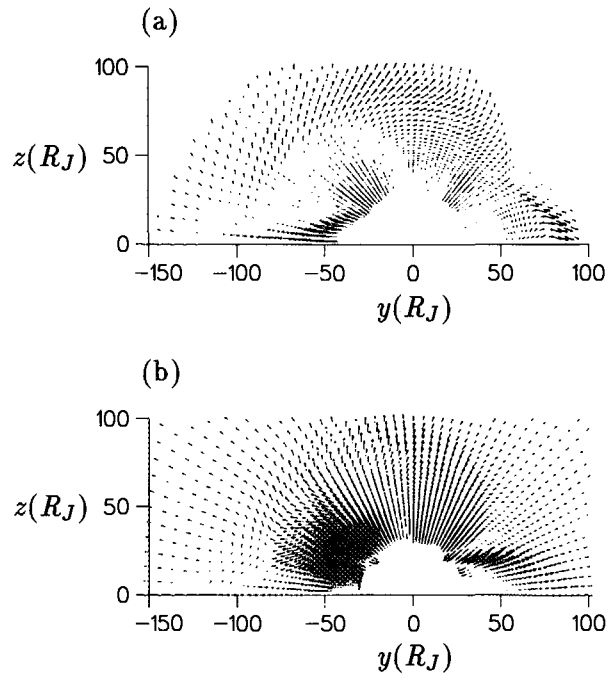
This is a blank page.

(a)

(b)

Figure 26: The vectors of (a) the plasma flow perpendicular to the magnetic field and (b) the total plasma flow on $x = 0$ plane in the case L. Here, the blue and the red arrows indicate the sunward and the anti-sunward flows, respectively
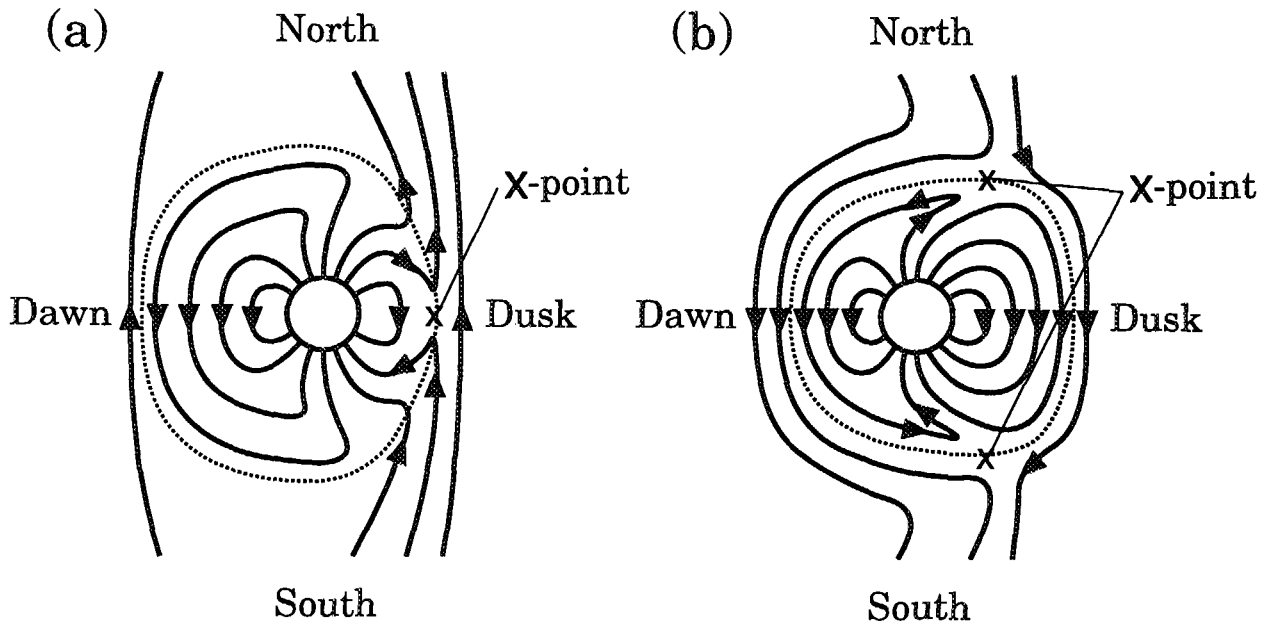
This is a blank page.

Figure 27: The schematic diagram of the cross section of the Jovian magnetospheric model on $x = 0$ plane (a) interacting with the northward IMF and (b) with the southward IMF, respectively. Here the dotted line shows the magnetopause.

This is a blank page.

国際単位系 (SI) と換算表

表1 SI基本単位および補助単位

量	名 称	記 号
長 さ	メ ー ト ル	m
質 量	キ ロ グ ラ ム	kg
時 間	秒	s
電 流	ア ン ペ ア	A
熱力学温度	ケ ル ビ ン	K
物 質 量	モ ル	mol
光 度	カ ン デ ラ	cd
平 面 角	ラ ジ ア ン	rad
立 体 角	ステラジアン	sr

表3 固有の名称をもつSI組立単位

量	名 称	記号	他のSI単位による表現
周 波 数	ヘ ル ツ	Hz	s^{-1}
力	ニ ュ ー ト ン	N	$m \cdot kg/s^2$
圧 力 ， 応 力	パ ス カ ル	Pa	N/m^2
エネルギー,仕事,熱量	ジ ュ ー ル	J	$N \cdot m$
工 率 ， 放 射 束	ワ ッ ト	W	J/s
電 気 量 ， 電 荷	ク ー ロ ン	C	$A \cdot s$
電位, 電圧, 起電力	ボ ル ト	V	W/A
静 電 容 量	フ ァ ラ ド	F	C/V
電 気 抵 抗	オ ー ム	Ω	V/A
コンダクタンス	ジ ー メ ン ス	S	A/V
磁 束	ウ ェ ー バ	Wb	$V \cdot s$
磁 束 密 度	テ ス ラ	T	Wb/m^2
インダクタンス	ヘ ン リ ー	H	Wb/A
セルシウス温度	セルシウス度	℃	
光 束	ル ー メ ン	lm	$cd \cdot sr$
照 度	ル ク ス	lx	lm/m^2
放 射 能	ベ ク レ ル	Bq	s^{-1}
吸 収 線 量	グ レ イ	Gy	J/kg
線 量 当 量	シ ー ベ ル ト	Sv	J/kg

表2 SIと併用される単位

名 称	記 号
分， 時， 日	min, h, d
度， 分， 秒	°, ′, ″
リ ッ ト ル	l, L
ト ン	t
電 子 ボ ル ト	eV
原子質量単位	u

$1\,eV = 1.60218 \times 10^{-19}\,J$

$1\,u = 1.66054 \times 10^{-27}\,kg$

表4 SIと共に暫定的に維持される単位

名 称	記 号
オングストローム	Å
バ ー ン	b
バ ー ル	bar
ガ ル	Gal
キ ュ リ ー	Ci
レ ン ト ゲ ン	R
ラ ド	rad
レ ム	rem

$1\,Å = 0.1\,nm = 10^{-10}\,m$

$1\,b = 100\,fm^2 = 10^{-28}\,m^2$

$1\,bar = 0.1\,MPa = 10^5\,Pa$

$1\,Gal = 1\,cm/s^2 = 10^{-2}\,m/s^2$

$1\,Ci = 3.7 \times 10^{10}\,Bq$

$1\,R = 2.58 \times 10^{-4}\,C/kg$

$1\,rad = 1\,cGy = 10^{-2}\,Gy$

$1\,rem = 1\,cSv = 10^{-2}\,Sv$

表5 SI接頭語

倍数	接頭語	記 号
10^{18}	エ ク サ	E
10^{15}	ペ タ	P
10^{12}	テ ラ	T
10^{9}	ギ ガ	G
10^{6}	メ ガ	M
10^{3}	キ ロ	k
10^{2}	ヘ ク ト	h
10^{1}	デ カ	da
10^{-1}	デ シ	d
10^{-2}	セ ン チ	c
10^{-3}	ミ リ	m
10^{-6}	マ イ ク ロ	μ
10^{-9}	ナ ノ	n
10^{-12}	ピ コ	p
10^{-15}	フ ェ ム ト	f
10^{-18}	ア ト	a

（注）

1. 表1－5は「国際単位系」第5版, 国際度量衡局 1985年刊行による。ただし, 1 eV および 1 u の値は CODATA の1986年推奨値によった。
2. 表4には海里, ノット, アール, ヘクタールも含まれているが日常の単位なのでここでは省略した。
3. bar は, JIS では流体の圧力を表わす場合に限り表2のカテゴリーに分類されている。
4. EC閣僚理事会指令では bar, barn および「血圧の単位」mmHg を表2のカテゴリーに入れている。

換 算 表

力	N($=10^5$ dyn)	kgf	lbf
	1	0.101972	0.224809
	9.80665	1	2.20462
	4.44822	0.453592	1

粘 度 $1\,Pa \cdot s(N \cdot s/m^2) = 10\,P(ポアズ)(g/(cm \cdot s))$

動粘度 $1\,m^2/s = 10^4 St(ストークス)(cm^2/s)$

圧力	MPa($=10$ bar)	kgf/cm²	atm	mmHg(Torr)	lbf/in²(psi)
	1	10.1972	9.86923	7.50062×10^3	145.038
	0.0980665	1	0.967841	735.559	14.2233
	0.101325	1.03323	1	760	14.6959
	1.33322×10^{-4}	1.35951×10^{-3}	1.31579×10^{-3}	1	1.93368×10^{-2}
	6.89476×10^{-3}	7.03070×10^{-2}	6.80460×10^{-2}	51.7149	1

エネルギー・仕事・熱量	J($=10^7$ erg)	kgf·m	kW·h	cal(計量法)	Btu	ft·lbf	eV
	1	0.101972	2.77778×10^{-7}	0.238889	9.47813×10^{-4}	0.737562	6.24150×10^{18}
	9.80665	1	2.72407×10^{-6}	2.34270	9.29487×10^{-3}	7.23301	6.12082×10^{19}
	3.6×10^6	3.67098×10^5	1	8.59999×10^5	3412.13	2.65522×10^6	2.24694×10^{25}
	4.18605	0.426858	1.16279×10^{-6}	1	3.96759×10^{-3}	3.08747	2.61272×10^{19}
	1055.06	107.586	2.93072×10^{-4}	252.042	1	778.172	6.58515×10^{21}
	1.35582	0.138255	3.76616×10^{-7}	0.323890	1.28506×10^{-3}	1	8.46233×10^{18}
	1.60218×10^{-19}	1.63377×10^{-20}	4.45050×10^{-26}	3.82743×10^{-20}	1.51857×10^{-22}	1.18171×10^{-19}	1

$1\,cal = 4.18605\,J$ （計量法）

$= 4.184\,J$ （熱化学）

$= 4.1855\,J$ （15 ℃）

$= 4.1868\,J$ （国際蒸気表）

仕事率 1 PS (仏馬力)

$= 75\,kgf \cdot m/s$

$= 735.499\,W$

放射能	Bq	Ci
	1	2.70270×10^{-11}
	3.7×10^{10}	1

吸収線量	Gy	rad
	1	100
	0.01	1

照射線量	C/kg	R
	1	3876
	2.58×10^{-4}	1

線量当量	Sv	rem
	1	100
	0.01	1